EUROFUSION WP15ER-PR(16) 16022

L Colas et al.

Spatial proximity effects on the excitation of Sheath RF Voltages by evanescent Slow Waves in the Ion Cyclotron Range of Frequencies.

Preprint of Paper to be submitted for publication in
Plasma Physics and Controlled Fusion

This work has been carried out within the framework of the EUROfusion Consortium and has received funding from the Euratom research and training programme 2014-2018 under grant agreement No 633053. The views and opinions expressed herein do not necessarily reflect those of the European Commission.

Spatial proximity effects on the excitation of Sheath RF Voltages by evanescent Slow Waves in the Ion Cyclotron Range of Frequencies.

Laurent Colas[1,a], Ling-Feng Lu[1], Alena Křivská[2], Jonathan Jacquot[3], Julien Hillairet[1], Walid Helou[1], Marc Goniche[1], Stéphane Heuraux[4] and Eric Faudot[4].

[1]*CEA, IRFM, F-13108 Saint-Paul-Lez-Durance, France.*

[2]*LPP-ERM-KMS, TEC partner, Brussels, Belgium.*

[3]*Max-Planck-Institut für Plasmaphysik, Garching, Germany.*

[4]*Institut Jean Lamour, UMR 7198, CNRS-University of Lorraine, F-54506 Vandoeuvre Cedex, France.*

[a)] Corresponding author: laurent.colas@cea.fr

Keyword: magnetic fusion devices, waves in ion cyclotron range of frequency, scrape-off layer, slow wave evanescence, radio-frequency sheath oscillations, sheath rectification, Green's functions

Abstract. We investigate theoretically how sheath radio-frequency (RF) oscillations relate to the spatial structure of the near RF parallel electric field $E_{//}$ emitted by Ion Cyclotron (IC) wave launchers. We use a simple model of Slow Wave (SW) evanescence coupled with Direct Current (DC) plasma biasing *via* sheath boundary conditions in a 3D parallelepiped filled with homogeneous cold magnetized plasma. Within a "wide sheaths" asymptotic regime, valid for large-amplitude near RF fields, the RF part of this simple RF+DC model becomes linear: the sheath oscillating voltage V_{RF} at open field line boundaries can be expressed as a linear combination of individual contributions by every emitting point in the input field map. SW evanescence makes individual contributions all the larger as the wave emission point is located closer to the sheath walls. The decay of $|V_{RF}|$ with the emission point/sheath poloidal distance involves the transverse SW evanescence length and the radial protrusion depth of lateral boundaries. The decay of $|V_{RF}|$ with the emitter/sheath parallel distance is quantified as a function of the parallel SW evanescence length and the parallel connection length of open magnetic field lines. For realistic geometries and target SOL plasmas, poloidal decay occurs over a few centimeters. Above this critical length, the poloidal structures of V_{RF} reflect those of $E_{//}$ near the parallel extremities of the input field map. Typical parallel decay lengths for $|V_{RF}|$ are found smaller than IC antenna parallel extension. Oscillating sheath voltages at IC antenna side limiters are therefore mainly sensitive to $E_{//}$ emission by active or passive conducting elements near these limiters, as suggested by recent experimental observations. Parallel proximity effects could also explain why sheath oscillations persist with antisymmetric strap toroidal phasing, despite the parallel anti-symmetry of the radiated field map. They could finally justify current attempts at reducing the RF fields induced near antenna boxes to attenuate sheath oscillations in their vicinity.

1. CONTEXT AND MOTIVATIONS

In magnetic fusion devices, non-linear wave-plasma interactions in the Scrape-Off Layer (SOL) often set operational limits for Radio-Frequency (RF) heating systems *via* impurity production or excessive heat loads [Noterdaeme1993]. Peripheral Ion Cyclotron (IC) power losses are generally attributed to RF sheath rectification. How this non-linear process depends on the geometry and electrical settings of the IC wave launchers remains largely unknown, despite crucial technological implications. In low-frequency small capacitive plasma discharges, sheath rectification has been successfully modelled in analogy with a double Langmuir probe driven by an oscillating voltage $\tilde{V}$ [Chabert2011]. In the absence of more elaborate theory in realistic tokamak geometry over large scale lengths, this simple formalism was also widely applied near IC antennas, without strong justification (e.g. in [Perkins1989]). Along this line of thought, the RF field parallel to the confinement magnetic field $\mathbf{B_0}$, integrated along isolated open magnetic field lines, $\tilde{V}=|\int E_{//}.dl|$, has often been used as a quantitative indicator of local RF sheath intensity in the vicinity of IC antennas, e.g. in [D'Ippolito1998], [Colas2005], [Mendes2010], [Garrett2012], [Milanesio2013], [Qin2013], [Campergue2014]. In this exercise one often uses $E_{//}$ fields from full-wave linear electromagnetic simulations where the plasma is in direct contact with metallic walls (i.e. without sheaths) [Milanesio2009] [Jacquot2015].

In tokamak experiments, qualitative correlation was noticed between the evolution of $\tilde{V}=|\int E_{//}.dl|$ and that of heat load intensity [Colas2009], [Campergue2014] or plasma radiation [Qin2013] [Colas2009]. Yet recent tokamak measurements challenge the relevance of $\tilde{V}$ as an indicator of RF sheath intensity. For example the line integral is expected to vanish in presence of a RF field map anti-symmetric along the parallel direction. This is nearly the case with anti-symmetric toroidal phasing of the IC poloidal strap arrays. Although the wave-plasma peripheral interaction is experimentally weaker with two straps phased $[0,\pi]$ than with [0,0] phasing [Colas2009], [Bobkov2015], it is not suppressed. Similar experimental results were obtained with more straps [Lerche2009], [Jacquet2011], [Jacquet2013], [Wukitch2013]. The magnetic field pitch with respect to the toroidal direction is often invoked to interpret the persistence of RF sheaths, in particular near antenna box corners, where tilted magnetic field lines do not pass in front of all the straps [Colas2005]. However on ASDEX-Upgrade, closing the box corners with metallic triangles did not suppress the local impurity production [Bobkov2010]. To mitigate the effect of magnetic field pitch, a field-aligned antenna was designed for ALCATOR C-mod. In comparison with a toroidally-aligned antenna, it was

predicted to reduce $|\tilde{V}|$ on open flux tubes with large toroidal extension on either sides of the IC wave launcher ("long field lines") [Garrett2012]. The expected reduction was significant with [0000] phasing of the 4-strap array. Experimental comparisons on ALCATOR C-mod revealed a reduced Molybdenum contamination when using the field-aligned antenna [Wukitch2013]. But the plasma potential measured on magnetic field lines connected to the antenna hardly varied, and the wave-SOL interaction was not suppressed with [0000] strap phasing.

At CEA, a prototype Faraday Screen (FS) was designed to reduce $|\tilde{V}|$ over "long field lines", by interrupting all parallel RF current paths on its front face [Mendes2010]. When compared to an antenna equipped with standard FS on Tore Supra (TS), the new FS exhibited similar heat load spatial distribution, but the measured RF wave-SOL interaction was more intense and more extended radially [Colas2013]. In a series of TS experiments, the left-right ratio of strap voltage amplitudes was varied by different means. Over this scan, the antenna side limiter near the strap with higher voltage heated up, while the remote limiter cooled down. A similar toroidal dissymetrization on ASDEX Upgrade produced opposite variations of shunt RF current amplitudes measured at two opposite antenna limiters [Bobkov2015]. In this experiment with $[0,\pi]$ phasing, in order to minimize the collected RF current, the RF voltage imposed on the remote strap was approximately twice higher than the voltage on the strap near the side limiter. These trends can hardly be explained using a single physical parameter simultaneously relevant at both extremities of the same open magnetic field line, $\tilde{V}$ or any other one. Besides, in the expression of $\tilde{V}$, all the points along the integration path play the same role. The experimental observations rather suggest that the toroidal distance between radiating elements and the observed walls might play a role in the RF-sheath excitation. From this paradigm, an alternative heuristic procedure was proposed to mitigate RF-sheath generation on new ASDEX-Upgrade antennas, by minimizing the local RF electric field amplitudes near the antenna limiters, still evaluated in the absence of RF sheaths [Bobkov2015]. This alternative procedure also deserves justification from first principles.

The "double probe" analogy implicitly assumes that each open magnetic field line behaves as electrically isolated from its neighbors. This is questionable in highly conductive plasmas, although the conductivity is far larger along $\mathbf{B_0}$ than transverse to it. The exchange of currents between neighboring flux tubes likely decouples the sheaths at the two extremities of the same open field line, as attest early attempts at improving the "double-probe" models [Rozhansky1998], [NGadjeu2011], [Faudot2013], [Jacquot2011]. The self-consistent spatio-temporal description of RF electric fields and RF currents, i.e. electrodynamics, has been long

developed in the context of IC antennas radiating in magnetized plasmas, but in the absence of sheaths [Milanesio2009], [Jacquot2015], [Lu2016a]. The RF plasma conductivity is then incorporated in a time-dispersive dielectric tensor [Stix1992]. Unlike capacitive RF discharges, tokamak field maps feature spatially inhomogeneous RF electric fields in the quasi-neutral plasma surrounding the wave launchers [Colas2005], [Mendes2010], [Bobkov2010], [Garret2012]. The distances between radiating elements and observation points, parallel and transverse to $\mathbf{B_0}$, then arise naturally *via* the propagation of RF waves.

In magnetic Fusion devices, steady-state (DC) currents parallel and transverse to $\mathbf{B_0}$ have also been reported in various SOL self-biasing experiments by sheath rectification near active IC antennas [VanNieuwenhove1992], [Gunn2008], [Bobkov2010]. With a non-linear I-V characteristic, sheaths couple RF and DC fields. On the one hand sheaths behave for RF waves as dielectric layers between the main plasma and the conducting walls, whose thickness depends on the DC sheath voltage. On the other hand, rectification of oscillating sheath voltages produces a self-biasing of the DC SOL plasma by RF waves. Coupling RF wave propagation and DC plasma biasing *via* non-linear RF and DC sheath boundary conditions, within a minimal model closer to the first principles, motivated the development of the Self-Consistent Sheath and Waves for Ion Cyclotron Heating (SSWICH) code [Colas2012], [Jacquot2014]. Similar models were developed in [Kohno2012], [Jenkins2015] but presently they do not allow the circulation of DC currents in the SOL. Besides, Kohno's RfSOL model cannot presently handle realistic antennas.

Realistic SSWICH simulations of the Tore Supra antenna environment, limited to the Slow Wave (SW), already reproduced qualitatively the left-right asymmetric heat loads and other experimental observations [Jacquot2014]. Similar efforts are underway to interpret the ASDEX-Upgrade measurements [Křivská2015] [Jacquot2015]. In SSWICH-SW simulations of the ITER antenna, parallel proximity effects were already evidenced numerically, but not interpreted [Colas2014]. Using the SSWICH-SW formalism, within restrictive assumptions on simulation domain shape, radial profiles, wave amplitude and polarization, this paper evidences and quantifies such asymmetries, explaining why they appear. Calculus is easier in a "wide sheath" regime, for which the excitation of sheath RF oscillations becomes a linear problem. Within this asymptotic limit, valid for intense DC biasing, the amplitude of the sheath oscillating voltages can be quantified as a *weighted* integral of $E_{//}$. This offers an alternative to $\tilde{V}$ for assessing RF-sheath excitation, with stronger theoretical justification. In the integral, proximity effects arise from the spatial dependence of the weight function (a Green's function for the linear problem). The SW evanescence between its emission point

and the sheath spatial location appears to strongly affect this spatial dependence. After briefly recalling the SSWICH-SW formalism, the paper investigates the Green's functions in two and three dimensions for a parallelepipedic simulation domain filled with homogeneous plasma and $\mathbf{B_0}$ normal to the lateral walls. The geometrical properties of the Green's functions are quantified using characteristic scale-lengths of the problem. In light of this new model we finally re-interpret the experimental observations summarized above. Concrete implications of the results are discussed, as well as some limitations of the proposed model.

2. COUPLING SLOW WAVE PROPAGATION AND DC PLASMA BIASING BY RADIO-FREQUENCY (RF) SHEATHS

2.1 Outline of SSWICH-SW asymptotic model

Our minimal model of coupled RF wave propagation and DC plasma biasing, SSWICH-SW, was detailed in references [Colas2012], [Jacquot2014] and is briefly summarized here. The simulation domain, sketched on Figure 1, features a collection of straight open magnetic flux tubes in a slab idealization of a tokamak SOL plasma. Two versions of the geometry will be used: a three dimensional (3D) model with boundaries parallel to the poloidal direction (y); as well as a 2D cut into the above 3D model along the radial direction (x) and parallel to the confinement magnetic field $\mathbf{B_0}$ (direction z). Both simulation domains are filled with cold magnetized plasma homogeneous along direction y, with possibly radial variation. Inner and outer boundaries of the domain are normal to x, while material boundaries of the fusion device are either parallel or normal to $\mathbf{B_0}$. This allows versatile geometries with radial profiles of the plasma parameters and private SOLs, sketched as gray levels, as well as protruding material objects, e.g. IC antenna side limiters (see [Jacquot2014]), intercepting the magnetic field lines and developing sheaths.

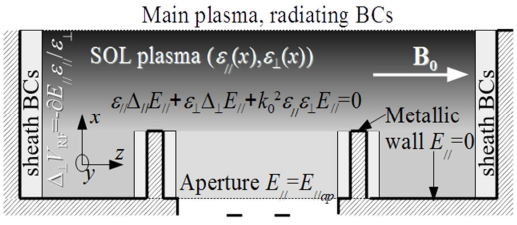

FIGURE 1: 2D (radial/parallel) cut into SSWICH general 3D simulation domain (not to scale). Main equations and notations used in the paper. The gray levels are indicative of the local plasma density. Light gray rectangles on boundaries normal to $\mathbf{B_0}$ feature the presence of sheaths, treated as boundary conditions in our formalism.

In this domain, the simulation process couples 3 steps self-consistently.

Step 1: Slow Wave propagation. The physical system is excited by a 2D (toroidal, poloidal) map of the complex parallel RF electric field $E_{//ap}(y,z)$, radiated by an IC antenna and prescribed at an aperture in the outer radial boundary of the simulation domain. The input RF field map presently needs to be computed *a-priori*, generally without sheaths, by an external antenna code. It carries the information about antenna geometry and its electrical settings. From the aperture, a time-harmonic cold Slow magneto-sonic Wave (SW) with pulsation ω_0 propagates across the whole simulation domain according to equation [Stix1992]

$$\varepsilon_\perp \Delta_\perp E_{//} + \varepsilon_{//} \Delta_{//} E_{//} + k_0^2 \varepsilon_{//} \varepsilon_\perp E_{//} = 0 \qquad (1)$$

With $\Delta_{//}.=\partial_{zz}{}^2.$ the parallel Laplace operator, $k_0=\omega_0/c$ the vacuum wavenumber, and $(\varepsilon_{//},\varepsilon_\perp)$ the diagonal elements of the local cold plasma dielectric tensor [Stix1992].

In 3D $\Delta_\perp.=\partial_{xx}{}^2.+\ \partial_{yy}{}^2.$, while in 2D $\Delta_\perp.=\partial_{xx}{}^2.-k_y{}^2$, where k_y is a wavevector in the ignorable (poloidal) direction y. These transverse derivatives couple adjacent magnetic field lines, unlike the simplest "double probe" models. Equation (1) is subject to radiating conditions at the inner radial boundary, metallic conditions $E_{//} = 0$ on material boundaries parallel to $\mathbf{B_0}$, and RF sheath boundary conditions (RF SBCs) at the parallel boundaries (see Figure 1). RF SBCs, first proposed in reference [D'Ippolito2006], will be further discussed.

Step 2: RF oscillations of the sheath voltage. When reaching the extremities of the open magnetic field lines, the SW fields $E_{//}$ generate oscillations V_{RF} of the sheath voltage at the RF pulsation ω_0. V_{RF} is generally a complex quantity incorporating amplitude and phase information. The definition $\mathbf{E}_\perp=\pm\boldsymbol{\nabla}_\perp V_{RF}$ at the sheath/plasma interface, combined with the relation $\nabla.(\boldsymbol{\varepsilon}\mathbf{E})=0$ valid all over the plasma, using $\mathbf{rot}_\perp\mathbf{E}_\perp=\mathbf{0}$ for the SW, yield a diffusion equation for the sheath oscillating voltages V_{RF} along the boundaries normal to $\mathbf{B_0}$, including a source term due to the SW [Colas2012],

$$\begin{aligned} &\varepsilon_\perp \Delta_\perp V_{RF}(x,y,z_{wall}) = \mp\varepsilon_{//}\partial_{//}E_{//}(x,y,z_{wall}) \\ &V_{RF}(x,y,z_{wall}) = 0 \text{ at boundary extremities} \end{aligned} \qquad (2)$$

Since the quantity V_{RF} is only meaningful at sheaths, equation (2) applies only at the domain boundaries normal to $\mathbf{B_0}$ (see figure (1)).

Step 3: Rectification of the sheath oscillations. Due to the non-linear I-V characteristics of the sheath, the RF oscillations of the sheath voltage are rectified into enhanced DC biasing of the SOL plasma. Several DC biasing models exist in the literature. These will not be detailed here, but the DC plasma potential V_{DC} is an increasing function of

the RF voltage amplitudes $|V_{RF}|$. The DC voltage drop across the sheaths affects their width *via* the Child Langmuir law, and consequently their RF admittance and the RF SBCs applied for $E_{//}$ [D'Ippolito2006]. Therefore all steps defined above generally need to be iterated till convergence is reached [Jacquot2014]. However for sheaths wider than a characteristic value, the RF SBCs were found nearly independent of the sheath widths [Colas2012] [Kohno2012]. For $\mathbf{B_0}$ normal to the wall the asymptotic RF SBCs simplify into $E_{//}=0$. In realistic Tore Supra simulations with self-consistent sheath widths, the near RF fields were intense enough to approach this "wide sheath" asymptotic regime [Jacquot2014].

2.2 Green's function description of RF-sheath excitation in the "wide sheath" regime

If sheaths are wide, or alternatively if their widths are prescribed in a non-self-consistent way [Myra2010], steps 1-3 are successive rather than coupled self-consistently. Besides, while step 3 is intrinsically non-linear, equations (1) and (2) are linear, together with their asymptotic BCs. In reference [Colas2012] a semi-analytic solution to this 3D linear sub-problem was proposed using sinusoidal eigenmodes of a plasma-filled rectangular box, as well as an iterative procedure for solving the fully-coupled non-linear problem. Antisymmetric eigenmodes were already shown to excite sheath oscillations, despite $\int E_{//}.dl$ being null in the quasi-neutral plasma. In more realistic 2D geometry, the Finite Element Method was applied in reference [Jacquot2014]. Here an alternative method is followed. Whatever the simulation domain, the superposition principle indeed allows expressing formally $V_{RF}(\mathbf{r})$ evaluated at any sheath boundary point $\mathbf{r}$ as the linear combination of elementary contributions by every emitting point at position $\mathbf{r_0}$ in the input RF field map.

$$V_{RF}(\mathbf{r}) = \int_{aperture} G(\mathbf{r},\mathbf{r_0}) E_{//\,ap}(\mathbf{r_0}) \mathbf{dr_0} \qquad (3)$$

Relation (3) formally looks like the integral $\tilde{V}=\int E_{//}.dl$ used in the "double probe" model, with major differences however. 1°) $V_{RF}(\mathbf{r})$ relates to one sheath, whereas $\tilde{V}$ was applied between two electrodes. Depending on the parallel symmetry of the input RF field map, the two extremities of the same open field line can now oscillate differently. 2°) Rather than along each open field line, integration is now performed over the aperture, either in 1D or 2D depending on the considered geometry. 3°) A weighting factor $G(\mathbf{r},\mathbf{r_0})$ is applied to $E_{//ap}(\mathbf{r_0})$, depending on the parallel and transverse distances from the field emission point $\mathbf{r_0}$ to the observation point $\mathbf{r}$ at the sheath walls.

$G(\mathbf{r},\mathbf{r_0})$ is the solution of equations (1) and (2) with elementary excitation $E_{//ap}(\mathbf{r})=\delta(\mathbf{r}-\mathbf{r}_0)$, i.e. a Green's function of the linear problem with one point source switched on in the input field map. $G(\mathbf{r},\mathbf{r_0})$ only carries information on the geometry of the simulation domain and on the SOL plasma parameters, while the input field map $E_{//ap}(\mathbf{r_0})$ accounts for the antenna properties. $V_{RF}(\mathbf{r})$ combines the two characteristics. Since the elementary source $\delta(\mathbf{r}-\mathbf{r}_0)$ can always be decomposed into a series of sinusoidal spatial components, a formal Fourier correspondence exists between the Green's function approach and the spectral method in [Colas2012]. While the formalism in relation (3) applies for complex geometries, in presence of radial density gradients and prescribed sheath widths, in the most general case the Green's functions can only be obtained numerically. The singularity in the RF electric field map related to the Dirac distribution makes this numerical task challenging. Consequently the Green's function formalism is generally less efficient than alternative methods to calculate oscillating voltages, unless the input field map is close to a Dirac distribution. Its main merit is to characterize explicitly the relation of $V_{RF}(\mathbf{r})$ to the spatial structure of the SW field. In order to get insight into these geometrical properties we treat below simple cases that are tractable semi-analytically.

3. PROXIMITY EFFECTS ON THE EXCITATION OF SHEATH RF VOLTAGES BY EVANESCENT SLOW WAVES IN 2D

To ease semi-analytical calculations, we restrict first the formalism to a 2-dimensional (2D) rectangular domain of dimensions $(L_{//}, L_{\perp})$ in the (parallel, radial) directions, filled with cold magnetized plasma homogeneous in all directions. In the ignorable direction y, spatial oscillations as $\exp(ik_y y)$ are assumed for RF quantities. The geometry is summarized in figure 2. The simulation domain is representative of the private SOL in front of an ICRF wave launcher, with $L_{\perp}$ the radial protrusion of (simplified !) antenna side limiters and $L_{//}$ the parallel distance between their internal faces. $E_{//}$ is prescribed at antenna aperture plane $x=0$. Radiating boundary conditions for $E_{//}$ are enforced at the inner boundary $x=L_{\perp}$, and asymptotic RF sheath BCs at parallel extremities $z=\pm L_{//}/2$.

Under these conditions relation (3) becomes

$$V_{RF}\left(x, z=\pm L_{//}/2\right)=\int_{-L_{//}/2}^{L_{//}/2} E_{//\,ap}(z_0)\,G_{2D}\left(x,k_y,\mp z_0\right)dz_0 \qquad (4)$$

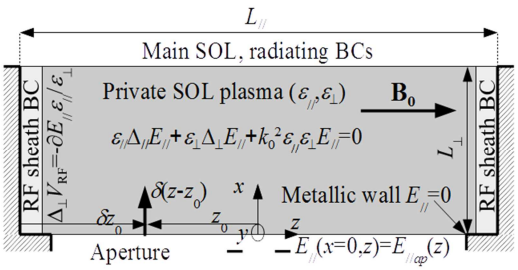

FIGURE 2: Generic 2D simulation domain (not to scale). Main equations and notations used in parts 3 and 4. x=0 at aperture. Light gray rectangles on boundaries normal to $\mathbf{B_0}$ feature the presence of sheath boundary conditions.

Green's function $G_{2D}(x,z_0)$ is non-dimensional and can be obtained from equations (1) and (2) at the left boundary with excitation $E_{//}(x=0,z)=E_{//ap}(z)=\delta(z-z_0)$ (see Figure 2). The sheath properties at the right boundary can be deduced by changing appropriate signs in (4). V_{RF} from relation (4) have the same magnitude at the two extremities of the same open magnetic field line only if the input field map is symmetric or anti-symmetric along $\mathbf{B_0}$.

3.1 Characteristic scale-lengths

Introducing characteristic squared lengths

$$L_x^2=\left[k_y^2-k_0^2\varepsilon_{//}\right]^{-1} \quad ; \quad L_z^2=\left[\varepsilon_{\perp}\left(k_y^2/\varepsilon_{//}-k_0^2\right)\right]^{-1}=L_x^2\varepsilon_{//}/\varepsilon_{\perp} \tag{5}$$

equation (1) can be recast into a standard form in the normalized space coordinates $X=x/|L_x|$ and $Z=z/|L_z|$

$$s_x\partial_{XX}^2E_{//}+s_z\partial_{ZZ}^2E_{//}-s_xs_zE_{//}=0 \tag{6}$$

Where s_x (resp. s_z) are the signs of L_x^2 (resp. L_z^2). Four cases need to be distinguished, corresponding to the four combinations of signs. If both signs are the same, equation (6) is elliptic and describes propagative (negative signs) or evanescent waves (positive signs) qualitatively similar to those in ordinary dielectric materials (i.e. the anisotropy of the magnetized plasma is a matter of length stretching). If signs are opposite equation (6) becomes hyperbolic and describes propagating waves with resonant cone properties comparable to Lower Hybrid waves in tokamaks [Stix1992]. In practice, s_x<0 corresponds to unrealistically low densities for IC waves in the SOL of tokamaks, for which sheaths have no deleterious effects. For s_x>0, s_z is the sign of $\varepsilon_{\perp}$ and could possibly change over the SOL: s_z<0 prevails in a tenuous plasma that might exist in an IC antenna box. Numerical simulations in [Lu2016a] suggest that the electric field there exhibits small-scale features highly sensitive to parametric variations, so that geometrical properties of G_{2D} are likely equally sensitive. s_z>0 corresponds to typical plasma parameters measured in the SOL surrounding IC antennas on Tore Supra [Jacquot2014] and ASDEX-Upgrade [Křivská2015]. Below we study specifically

this latter case and treat L_x and L_z as real positive quantities. $\varepsilon_\perp$=0 corresponds to the Lower Hybrid resonance and is associated with very large L_z values. Equation (1) implicitly assumes a scale separation between the SW and the Fast Wave. Close to the Lower Hybrid resonance this separation needs to be revisited to allow a possible mode conversion between the two wave polarizations. This is however outside the scope of the present paper.

Lateral boundaries at finite distance from the emission points also introduce $L_{//}$ as a characteristic length of the wave propagation model. Excitation finally deserves normalization

$$E_{//ap}(z)=\delta(z-z_0)=L_z^{-1}\delta(Z-Z_0) \tag{7}$$

A similar dimensional analysis can be made for equation (2) at the left boundary, using the normalized coordinates defined for equation (1)

$$\partial^2_{XX}G_{2D}-k_y^2L_x^2G_{2D}=\partial_Z L_z E_{//} \tag{8}$$

where from (7) $L_zE_{//}$ is non-dimensional. Equation (8) introduces the extra scale-length k_y^{-1} into the problem, *via* the dimension-less parameter $k_y^2L_x^2=[1-k_0^2\varepsilon_{//}/k_y^2]^{-1}$. Besides, the boundary conditions involve $L_\perp$.

In principle, all the geometrical properties of $G_{2D}(x,k_y,z_0)$ can be expressed in terms of (x, z_0) and the characteristic lengths. Throughout the paper typical examples will illustrate our calculations, with realistic geometrical, plasma and RF parameters used for ASDEX-Upgrade simulations in [Křivská2015]. Dielectric properties correspond to a standard D[H] minority heating scheme at frequency f_0=30MHz, with local magnetic field B_0=1.44T and L-mode SOL density n_e=8.3×10^{17}m^{-3} in the antenna region. Geometry refers to ASDEX-Upgrade 2-strap antennas. Simulation parameters are $\varepsilon_{//}$=-74659, $\varepsilon_\perp$=-24.31, k_0=0.63m^{-1}, $L_{//}$=0.66m, $L_\perp$=12mm. For this particular case L_x=5.8248mm while L_z=0.3228m for k_y=0. For this realistic example, the parallel evanescence length is thus half the parallel extension of the antenna, while the transverse evanescence length is a small fraction of the poloidal height for the antenna.

3.2 2D electric field maps

The solution to equation (6) can be built from well-known results for the 2D Helmholtz equation in isotropic cylindrical geometry using modified Bessel functions of the second kind K_j (j integer [Angot1972]). The method of images [MF1953] is then applied to account for the parallel boundary conditions at finite distance from the emitting point. Using the normalized coordinates (X,Z) the field map writes

$$E_{2D}(x,z,z_0)=L_z^{-1}\sum_{n=-\infty}^{+\infty}(-1)^n F_{2D}(X,Z-Z_n) \quad ; \quad Z_n=\left[nL_{//}+(-1)^n z_0\right]/L_z \qquad (9)$$

Where

$$F_{2D}(X,Z)=\frac{X}{\pi R}\mathrm{K}_1(R) \quad ; \quad R^2=X^2+Z^2 \qquad (10)$$

Here argument R is the (normalized) distance to the emitting source. Function F_{2D}, plotted in 2D on Figure 3, describes the SW evanescence from a boundary point source in $(X,Z)=(0,0)$, in absence of parallel boundaries. For a fixed X and $Z>>X>1$, F_{2D} decays as ~exp(-Z) along the parallel direction. F_{2D} is null in $X=0$, except in $Z=0$ where the source term creates a singularity.

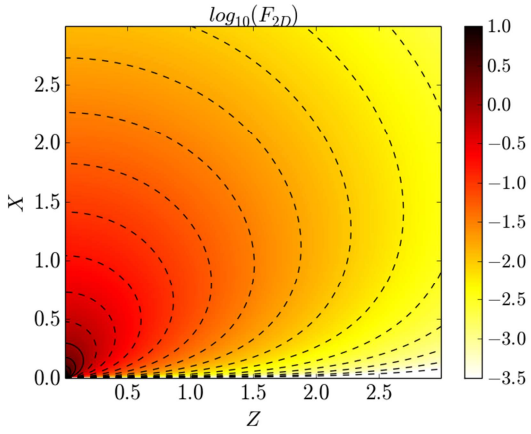

FIGURE 3. 2D plot of F_{2D}in logarithmic scale versus normalized coordinates (X,Z).

Figures 4 map E_{2D} versus (x,z) for the ASDEX-Upgrade simulation parameters in [Křivská2015] and various z_0, showing how the parallel position of the emitting point affects the spatial shape of the RF field maps. More specifically, the RF sheath voltage excitation in (2) depends on the parallel derivative $\partial_z E(x,z=\pm L_{//}/2,z_0)$, with

$$\begin{aligned}\partial_z E_{2D}(x,z,z_0)&=L_z^{-2}\sum_{n=-\infty}^{+\infty}(-1)^n\partial_Z F_{2D}(X,Z-Z_n)\\ \partial_Z F_{2D}(X,Z)&=-\frac{XZ}{\pi R^2}K_2(R)\end{aligned} \qquad (11)$$

Figures 4 show that this gradient is generally different at the two extremities of the same open magnetic field line, hence also the sheath RF voltages. From (4) one can actually anticipate that V_{RF} amplitudes vary in opposite ways as the parallel position z_0 of the emitting point is moved, qualitatively consistent with experimental observations in [Colas2013] and [Bobkov2015]. We now focus on the left boundary.

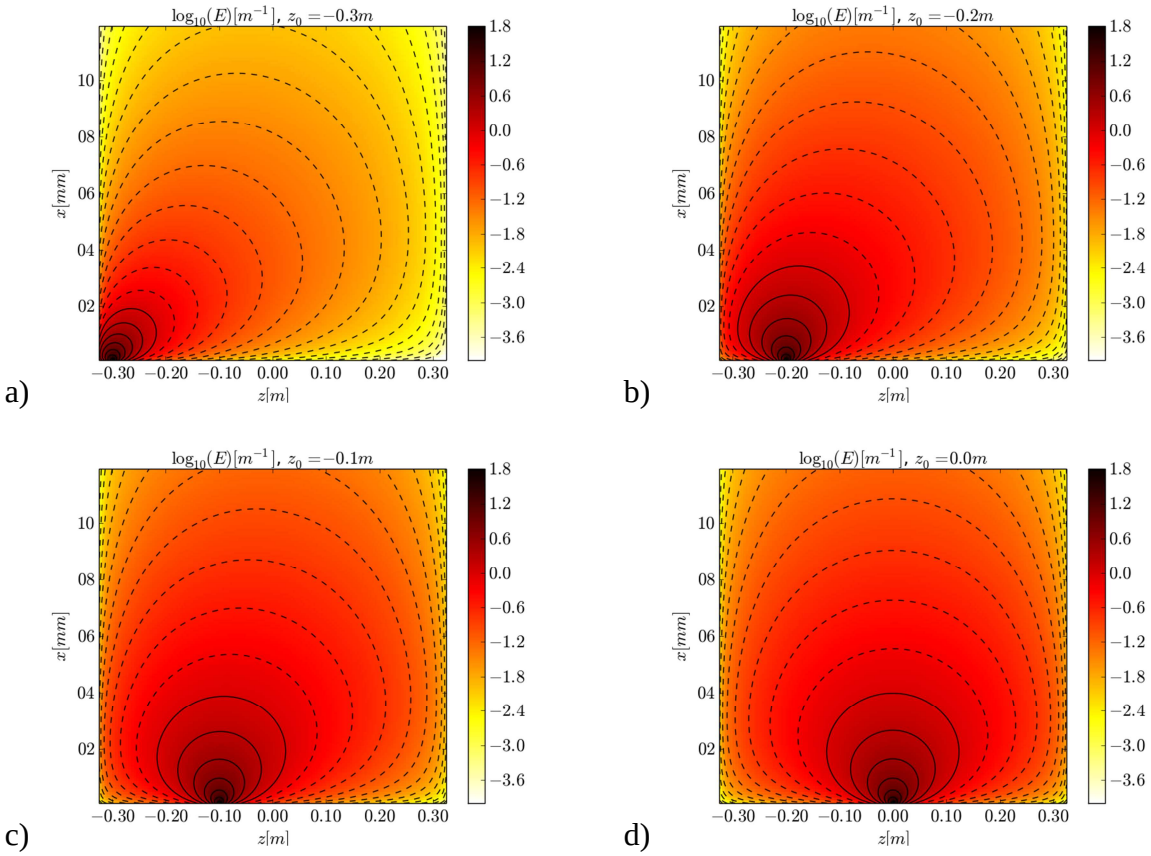

FIGURE 4. 2D (parallel/radial) maps of $E_{2D}(x,z,z_0)$ in logarithmic scale, for ASDEX-Upgrade simulation parameters in [Křivská2015]and (a) z_0=-30cm; (b) z_0=-20cm; (c) z_0=-10cm; (d) z_0=0cm. x=0 corresponds to the antenna aperture, and x increases towards main plasma. z=0 is the mid-plane between antenna side limiters at z=±0.33m

z_0=+$L_{//}$/2 corresponds to a source point near the right parallel boundary of the simulation domain. When z_0=+$L_{//}$/2 and z=-$L_{//}$/2, Z_{2p}=Z_{2p+1}, for all p integer in summation (9) whence

$$\partial_z E_{2D}\left(x,-L_{//}/2,+L_{//}/2\right)=0 \qquad (12)$$

When the source point gets very close to the left sheath wall it is convenient to introduce δZ_0=(z_0+$L_{//}$/2)/L_z, the normalized parallel distance from the source point z=z_0 to the left boundary z=-$L_{//}$/2 (see figure 2). For sufficiently small δZ_0, n=0 and n=-1 become the dominant terms in the summation (9)

$$\partial_z E_{2D}\left(x, z=-L_{//}/2, z_0\right) \approx 2L_z^{-2}\partial_Z F_{2D}\left(X,\delta Z_0\right)=\frac{2X\delta Z_0}{\pi R_0^2 L_z^2}K_2\left(R_0\right) \qquad (13)$$

Formula (13) shows that $\partial_z E_{2D}(x,z=-L_{//}/2,z_0)$ tends to 0, except perhaps in x=0, where R_0 vanishes. In the limit R<<1, $K_2(R)\sim 2/R^2$ [Angot1972] and

$$\partial_z E_{2D}\left(x, z=-L_{//}/2, z_0\right) \approx \frac{4X\delta Z_0}{\pi L_z^2\left[X^2+\delta Z_0^2\right]^2} \tag{14}$$

To shed light into the limit behavior $\delta Z_0 \to 0$, $X \to 0$ let us integrate with respect to X

$$\int_X^\infty \partial_z E_{2D}\left(x, z=-L_{//}/2, z_0\right) dX \approx \frac{2\delta Z_0}{\pi L_z^2\left[X^2+\delta Z_0^2\right]} \tag{15}$$

Integrating once again yields

$$\int_0^X \frac{2\delta Z_0}{\pi L_z^2\left[X'^2+\delta Z_0^2\right]} dX' = \frac{2}{\pi L_z^2}\arctan\left(\frac{X}{\delta Z_0}\right) \xrightarrow{\delta Z_0 \to 0} \frac{1}{L_z^2} \text{ whetever } X \tag{16}$$

Whence in the limit $\delta z_0 \to 0$, $x \to 0$

$$\partial_z E_{2D}\left(x, z=-L_{//}/2, z_0\right) \approx \frac{2}{L_z^2}\partial_X\, \delta(X) = 2\frac{\varepsilon_\perp}{\varepsilon_{//}}\partial_x\, \delta(x) \tag{17}$$

The limit δZ_0>>1, Z_1>>Z_0 is accessible if $L_{//}$>>L_z. Z_1>>Z_0 implies that n=0 and n=-1 are still the dominant terms in the summation (9), so that formula (15) applies. In the limit of large arguments $K_2(R)\sim[\pi/2R]^{1/2}\exp(-R)$ [Angot1972], so that

$$\partial_z E_{2D}\left(x, z=-L_{//}/2, z_0\right) \approx -\sqrt{\frac{2}{\pi}}\frac{X\delta Z_0}{L_z^2\left[X^2+\delta Z_0^2\right]^{5/2}}\exp\left[-\left(X^2+\delta Z_0^2\right)^{1/2}\right] \tag{18}$$

If δZ_0>>X>1, then $\partial_z E_{2D}(x,z=-L_{//}/2,z_0)$ decreases as $\sim\exp(-\delta z_0/L_z)$ as the source point moves away from the sheath wall. The characteristic length $L_{//}$ does not appear explicitly in expression (18). Indeed this length is related to the boundary conditions. Their effect on the Green's function is only significant if the source point z_0 is located within a distance L_z from the right hand side parallel boundary, which is a small zone in the limit $L_{//}$>>L_z. The distance to the right boundary is reflected in the requirement Z_1>>Z_0.

3.3 2D Green's function for the sheath oscillating voltage.

Inserting expression (9) into equation (2), one deduces $G_{2D}(x,k_y,z_0)$ as a convolution of $\partial_z E(x,-L_{//}/2,z_0)$ with a Green's function for the diffusion equation [Colas2012]:

$$G_{2D}\left(x,k_y,z_0\right)=\frac{\varepsilon_{//}}{\varepsilon_{\perp}}\int_0^{L_{\perp}}\partial_z E_{2D}\left(x',-L_{//}/2,z_0\right)\frac{\sinh\left(k_y x_{\min}\right)}{k_y}\frac{\sinh\left(k_y\left(L_{\perp}-x_{\max}\right)\right)}{\sinh\left(k_y L_{\perp}\right)}dx' \tag{19}$$

Where x_{min}=min(x,x') and x_{max}=max(x,x').

For the ASDEX-Upgrade parameters, Figures 5 plot G_{2D} versus x for two values of k_y and various parallel distances δz_0 between the emission point and the left wall. The boundary conditions in equation (2) impose $G_{2D}\left(0,k_y,z_0\right)=0$ and $G_{2D}\left(L_{\perp},k_y,z_0\right)=0$. Between these two radial extremities G_{2D} at fixed z_0 exhibits a radial maximum, whose position shifts radially inwards with increasing δz_0.

Figures 5 show that for fixed x G_{2D} decreases with increasing δz_0. This is a first evidence of parallel proximity effects in realistic tokamak conditions. SW evanescence ensures that this result is quite general: indeed $\partial_z E_{2D}(x,z=-L_{//}/2,z_0)$ is a decreasing function of z_0. From (19) one deduces that this is also the case for G_{2D}. When the source point moves towards the right wall formula (13) yields

$$G_{2D}\left(x,k_y,+L_{//}/2\right)=0 \tag{20}$$

The lower curves on Figure 5 reflect this trend. When the source point gets close to the left wall the limit behavior is deduced from formula (17)

$$\begin{aligned}G_{2D}\left(x,k_y,-L_{//}/2\right)&\approx 2\int_0^{L_{\perp}}\partial_{x'}\delta\left(x'\right)\frac{\sinh\left(k_y x_{\min}\right)}{k_y}\frac{\sinh\left(k_y\left(L_{\perp}-x_{\max}\right)\right)}{\sinh\left(k_y L_{\perp}\right)}dx'\\&=2\frac{\sinh\left(k_y\left(L_{\perp}-x\right)\right)}{\sinh\left(k_y L_{\perp}\right)}\int_0^{L_{\perp}}\delta\left(x'\right)\cosh\left(k_y x'\right)dx'=\frac{\sinh\left(k_y\left(L_{\perp}-x\right)\right)}{\sinh\left(k_y L_{\perp}\right)}\end{aligned} \tag{21}$$

Expression (21) corresponds to the dashed lines on figures 5.

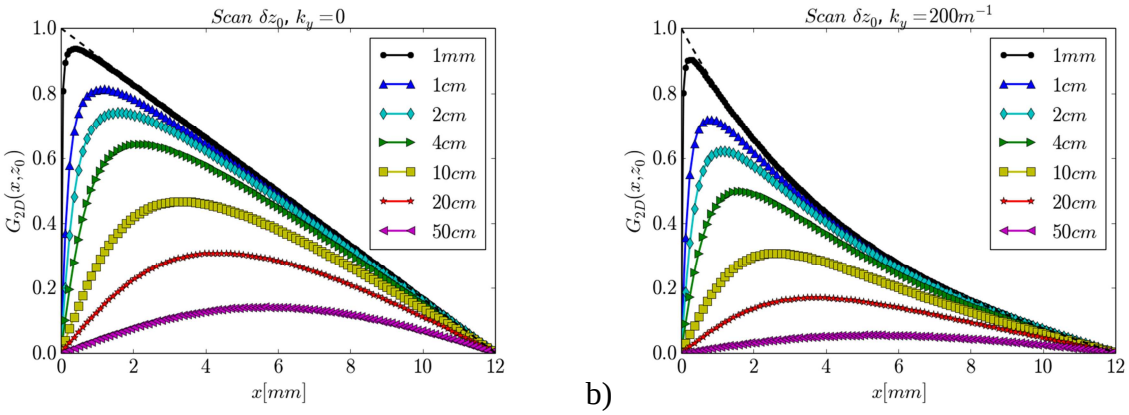

a) b)

FIGURE 5. Green's function $G_{2D}(x,k_y,z_0)$ *versus* radial coordinate x for increasing parallel distance $\delta z_0=(L_{//}/2+z_0)$ from wave emission point $z=z_0$ to left parallel boundary $z=-L_{//}/2$. x is 0 at aperture and increases towards leading edge of antenna limiter at $x=L_\perp=12$mm. Simulation with ASDEX-Upgrade parameters used in [Křivská2015] and (a) $k_y=0$, (b) $k_y=200\text{m}^{-1}$. Dashed lines: asymptotic expression (21).

From the two limit expressions (20) and (21), we deduce that $0\leq G_{2D}(x,z_0)\leq \sinh(k_y(L_{//}-x))/\sinh(k_yL_{//})\leq 1$: G_{2D} is a real positive attenuation factor.

The way G_{2D} decreases with δz_0 depends on the input parameters. To quantify these parallel proximity effects, a first indicator is the e-fold parallel decay length $\lambda_z(x)$ of $G_{2D}(x,k_y,z_0)$ at $z_0=0$. In a series of numerical simulations $\lambda_z(x)$ was fitted numerically for 20 values of x from 0 to $L_\perp$. Figure 6 plots $\lambda_z(x)$ averaged over x *versus* L_z, for various parametric scans, exhibiting two regimes. On the low-L_z branch of the curves, if $\delta Z_0 >> X$ while $Z_1>Z_0$, equation (18) shows that $\partial_z E(x,z=-L_{//}/2,z_0)$ decreases as $\sim\exp(-\delta z_0/L_z)$ for all x and so does $G_{2D}(x,k_y,z_0)$. A saturation of λ_z is however observed as L_z gets of the order of $L_{//}$. Over the scans of $\varepsilon_\perp$, the saturation level on this opposite branch is found proportional to $L_{//}$. Indeed if $L_{//}<<L_z$, $\delta Z_0<<1$ for all $\delta z_0<L_{//}$, but all terms matter *a priori* in summation (9). However all the relevant contributions to this summation can be linearized. Expression (20) then ensures that $G_{2D}(x,k_y,z_0)$ decreases linearly as $(1-\delta z_0/L_{//})$

$$G_{2D}(x,k_y,z_0) \approx G_{2D}(x,k_y,z_0=-L_{//}/2)\left(1-\frac{\delta z_0}{L_{//}}\right) = \frac{\sinh\left(k_y(L_\perp-x)\right)}{\sinh\left(k_yL_\perp\right)}\left(1-\frac{\delta z_0}{L_{//}}\right) \quad ; \quad L_{//}<<L_z \qquad (22)$$

Expression (22) shows that in the limit $L_{//}<<L_z$ the characteristic length L_z plays no role in the SSWICH-SW problem. From figure 6 and the above estimates, one concludes that $\lambda_z<\min(L_z,L_{//})$.

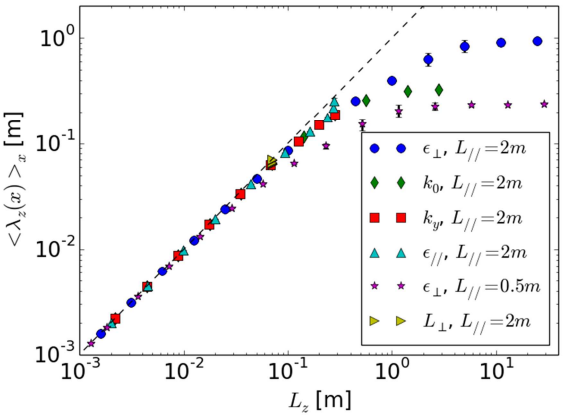

FIGURE 6. Parallel e-fold decay length $\lambda_z(x)$ of $G_{2D}(x,k_y,z_0)$ at $z_0=0$ fitted numerically and averaged over 20 values of x, versus L_z from eq. (5), for 6 scans of the main parameters in the asymptotic model, each identified by a marker type. Error bars: dispersion of $\lambda_z(x)$ over x.

Another quantitative indicator of parallel proximity effects, the parallel gradient length of G_{2D} at $\delta z_0=0$, is plotted on figure 7. Below we seek an upper bound on this gradient length. The parallel gradient of G_{2D} is expressed as

$$\partial_{z_0} G_{2D}(x,k_y,z_0)=\frac{\varepsilon_{//}}{\varepsilon_\perp}\int_0^{L_\perp}\partial^2_{zz_0}E_{2D}(x',-L_{//}/2,z_0)\frac{\sinh(k_y x_{\min})}{k_y}\frac{\sinh(k_y(L_\perp-x_{\max}))}{\sinh(k_y L_\perp)}dx' \tag{23}$$

Where $\partial^2_{zz0}E(x,-L_{//}/2,z_0)$ is built from

$$\partial_{ZZ}F_{2D}(X,Z)=-\frac{X}{\pi R^3}\left[RK_2(R)-Z^2K_3(R)\right] \tag{24}$$

From (23) and the above analysis one deduces that for $L_z<<L_{//}$, $\partial_{z0}G_{2D}$ scales as L_z^{-1} when all other parameters are kept constant, while for $L_z>>L_{//}$

$$\partial_{z_0} G_{2D}(x,k_y,z_0)\approx -G_{2D}(x,k_y,z_0=-L_{//}/2)/L_{//} \quad ; \quad L_{//}<<L_z \tag{25}$$

From figure 5 one also anticipates very steep gradients as x gets very small. One can show that an upper bound for G_{2D} gradient length is given by

$$\begin{aligned} L_{z\max} &= \min\left[\frac{\pi x}{2L_x}L_z, L_z/I\left(\frac{L_\perp}{L_x},k_yL_x\right), L_{//}\right] \\ I\left(\frac{L_\perp}{L_x},k_yL_x\right) &= 2\int_0^{L_\perp/L_x}\partial^2_{ZZ}F_{2D}(X,Z=0)\frac{\sinh(k_yL_xX)}{k_yL_x}dX \end{aligned} \tag{26}$$

Figure 7 illustrates numerically this upper bound over four orders of magnitude, for various scans of the main parameters in the SSWICH asymptotic model.

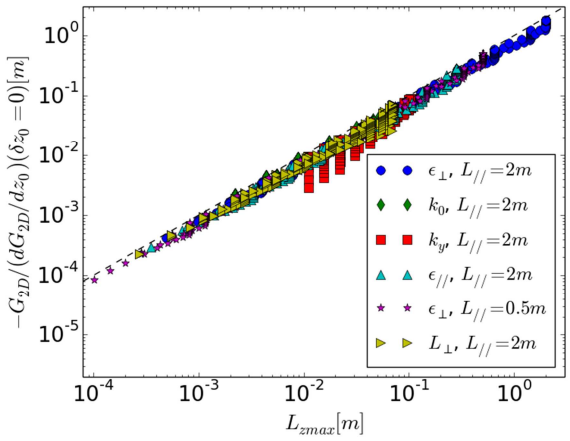

FIGURE 7. Parallel gradient length of $G_{2D}(x,k_y,z_0)$ fitted numerically at $\delta z_0=0$, *versus* upper bound L_{zmax} from eq. (26). For each simulation, 19 points are plotted, for x values located every 5% of $L_\perp$. Marker types indicate simulation series with one parameter scanned.

4. EXTENSION TO 3 DIMENSIONS

For more realistic description of the RF-sheath excitation, the Green's function formalism can be extended to 3D parallelepipedic simulation domains. Throughout this part the parallel and radial dimensions $L_{//}$ and $L_\perp$ are the same as in 2D, while the poloidal extent of the domain is infinite. The transverse Laplace operator is redefined as $\Delta_\perp.=\partial_{xx}{}^2.+\partial_{yy}{}^2$, while both $E_{//}$ and V_{RF} are assumed to vanish for $y\to\pm\infty$. Equation (3) now consists of a surface integral over a 2D input RF field map $E_{//ap}(y,z)$

$$V_{RF}(x,y,z=\pm L_{//}/2)=\int_{-\infty}^{+\infty}dy_0\int_{-L_{//}/2}^{L_{//}/2}E_{//ap}(y_0,z_0)G_{3D}(x,y-y_0,\mp z_0)dz_0 \qquad (27)$$

Here the 3D Green's function $G_{3D}(x,y,z_0)$ has the dimension of a wavevector, and is obtained for the elementary excitation $E_{//ap}(y,z)=\delta(y)\delta(z-z_0)$. The 3D model exhibits the same characteristic scale-lengths as the 2D model, except that $k_y=0$ is implicitly assumed, while coordinate y replaces the characteristic length k_y^{-1}.

4.1 Green's function in 3D

The 3D RF field pattern $E_{3D}(x,y,z,z_0)$ is obtained using the same method as in 2D. It is most easily expressed using the normalized quantities $X=x/L_x$, $Y=y/L_x$ and $Z=z/L_z$

$$E_{3D}(x,y,z,z_0)=L_x^{-1}L_z^{-1}\sum_{n=-\infty}^{+\infty}(-1)^n F_{3D}(X,Y,Z-Z_n)\quad;\quad Z_n=\left[nL_{//}+(-1)^n z_0\right]/L_z \qquad (28)$$

with

$$F_{3D}(X,Y,Z)=\frac{1}{2\pi}\frac{X(1+R)}{R^3}\exp(-R) \quad ; \quad R=\sqrt{X^2+Y^2+Z^2} \tag{29}$$

Figure 8 maps F_{3D} in Z=0 *versus* (X,Y). F_{3D} is null in X=0, except in Y=Z=0 where it exhibits a singularity. Decay as exp(-R) is found for large R.

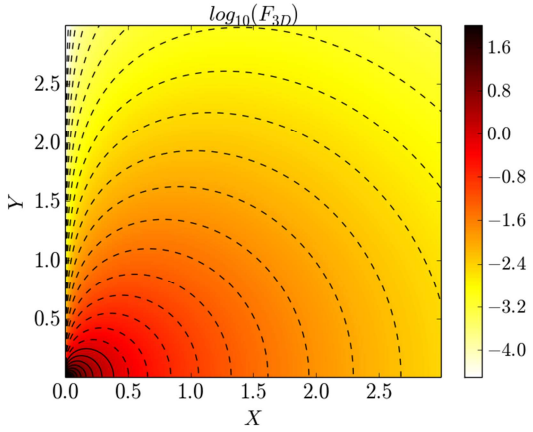

FIGURE 8. 2D (radial, poloidal) map of $F_{3D}(X,Y,Z=0)$ from formula (29) in logarithmic scale, versus normalized transverse coordinates (X, Y).

$\partial_z E_{3D}(x,y,z,z_0)$ is computed using

$$\partial_Z F_{3D}(X,Y,Z)=-\frac{XZ(3+3R+R^2)}{2\pi R^5}\exp(-R) \tag{30}$$

whence

$$G_{3D}(x,y,z_0)=\frac{\varepsilon_{//}}{\varepsilon_\perp}\int_{-\infty}^{+\infty}\int_0^{L_\perp}\partial_z E_{3D}(x',y',z=-L_{//}/2,z_0)H(x,x',y-y')dx'dy' \tag{31}$$

With the 2D solution of equation (2) given by [Durand1966] p.265

$$H(x,x',y)=\arg\tanh\left[\frac{\sin(\pi x/L_\perp)\sin(\pi x'/L_\perp)}{\cosh(\pi y/L_\perp)-\cos(\pi x/L_\perp)\cos(\pi x'/L_\perp)}\right] \tag{32}$$

Figures 9 map $G_{3D}(x,y,z_0)$ *versus* (x,y) as obtained numerically for the ASDEX-Upgrade simulation parameters and three values of δz_0. At given (x,z_0) G_{3D} is a decreasing function of the poloidal distance |y| from wave emission point to observation point. Over this scan V_{RF} at a given altitude involves the $E_{//ap}$ values within less than 1.5cm from this altitude. Figures 9 also illustrate how G_{3D} decreases in magnitude, expands in the poloidal direction while its radial maximum moves away from the aperture with increasing parallel distance from wave-emitting point to sheath wall. Let us now quantify these properties.

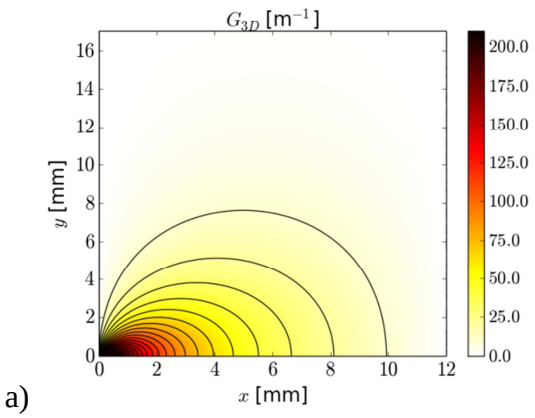

a)

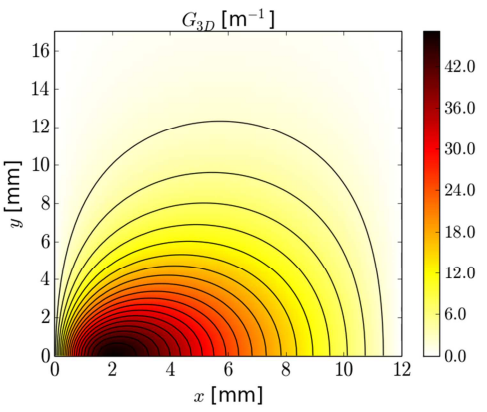

b)

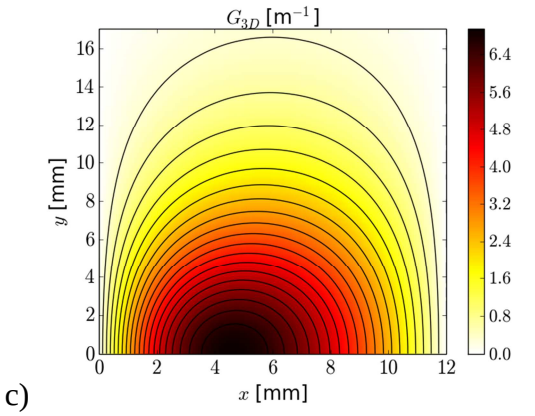

c)

FIGURE 9. 3D Green's function $G_{3D}(x,y,z_0)$ *versus* transverse coordinates (x,y), as evaluated numerically using ASDEX-Upgrade simulation parameters in [Křivská2015] and parallel distances (a) $\delta z_0=(L_{//}/2+z_0)=2.5$cm; (b) $\delta z_0=10$cm and (c) $\delta z_0=33$cm. Contour lines are located every 5% of the maximum value over the map.

4.2 Evolution with δz_0

SW evanescence ensures that G_{3D} decreases with δz_0 at fixed (x,y). Since $\delta(y)=\frac{1}{2\pi}\int_{-\infty}^{+\infty}\exp(ik_y y)dk_y$ the 2D and 3D Green's functions are Fourier transforms of each other

$$\begin{aligned} G_{3D}(x,y,z_0) &= \frac{1}{2\pi}\int_{-\infty}^{+\infty} G_{2D}(x,k_y,z_0)\exp(i\,k_y y)dk_y \\ &= \frac{1}{\pi}\int_{0}^{+\infty} G_{2D}(x,k_y,z_0)\cos(k_y y)dk_y \end{aligned} \qquad (33)$$

From our 2D analysis in part III, one deduces that G_{3D} is null for $z_0=+L_{//}/2$. In the opposite limit $z_0\rightarrow -L_{//}/2$, one gets from relation (21) [Gradshteyn1980] p.504

$$\begin{aligned} G_{3D}(x,y,-L_{//}/2) &\approx \frac{1}{2\pi}\int_{-\infty}^{+\infty}\frac{\sinh(k_y(L_\perp-x))}{\sinh(k_y L_\perp)}\exp(ik_y y)dk_y \\ &= \frac{1}{2L_\perp}\frac{\sin(\pi x/L_\perp)}{\cosh(\pi y/L_\perp)-\cos(\pi x/L_\perp)} \end{aligned} \qquad (34)$$

And if $L_z>>L_{//}$ while $Y^2<<1$, one anticipates a linear decay with parallel distance δz_0.

$$G_{3D}(x,y,z_0) \approx \frac{1-\delta z_0/L_{//}}{2L_\perp} \frac{\sin(\pi x/L_\perp)}{\cosh(\pi y/L_\perp)-\cos(\pi x/L_\perp)} \qquad (35)$$

Figure 10 illustrates the limit expression of $G_{3D}(x,y,-L_{//}/2)$ in (34). Since the emission point is infinitely close to the sheath wall, G_{3D} exhibits a singularity in $(x,y)=(0,0)$. No wave evanescence is involved: L_x and L_z disappear from the problem, all coordinates can be normalized by the only remaining characteristic length $L_\perp$.

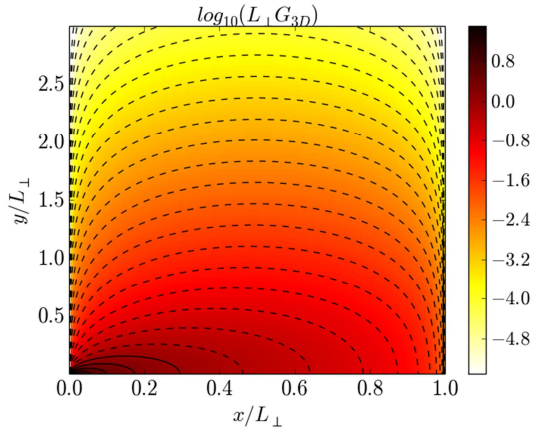

FIGURE 10. 2D (radial, poloidal) map of $L_\perp G_{3D}(x,y,-L_{//}/2)$ from formula (34) in logarithmic scale, versus normalized coordinates $(x/L_\perp, y/L_\perp)$.

Poloidal integration of G_{3D} yields

$$\int_{-\infty}^{+\infty} G_{3D}(x,y,z_0)dy = G_{2D}(x,k_y=0,z_0) \qquad (36)$$

From the 2D analysis, one deduces that for $\delta z_0/L_z >> (x^2+y^2)^{1/2}/L_x$ and $L_{//}/2-z_0 >> L_z^2$, the poloidal integral of G_{3D} decays as $\exp(-\delta z_0/L_z)$ for large δz_0. The upper bound L_{zmax} from expression (26) is also valid.

4.3 Poloidal decay lengths, relevance of 2D simulations

Surface integral (27) can be seen as a weighted sum of line integrals over several open magnetic flux tubes instead of one in the previous approaches. It is worth estimating how many of these open magnetic field lines do really matter in expression (27). A related issue is the validity of 2D SSWICH-SW simulations in part III in comparison with the more accurate, but more computationally demanding 3D simulations in part IV. This amounts to evaluating the poloidal extent of G_{3D} at fixed (x,z_0).

For $\delta z_0=0$ formula (34) features a minimal poloidal extent of G_{3D} in the absence of SW evanescence. The half-width at 1/e can be evaluated analytically as

$$\frac{\Delta y}{L_\perp} = \frac{1}{\pi} \mathrm{a\,cosh}\left[e + (1-e)\cos\left(\frac{\pi x}{L_\perp}\right)\right] \qquad (37)$$

Expression (37) is plotted on figure 11, showing that $\Delta y<0.7L_\perp$ over the whole radial range of the simulation domain.

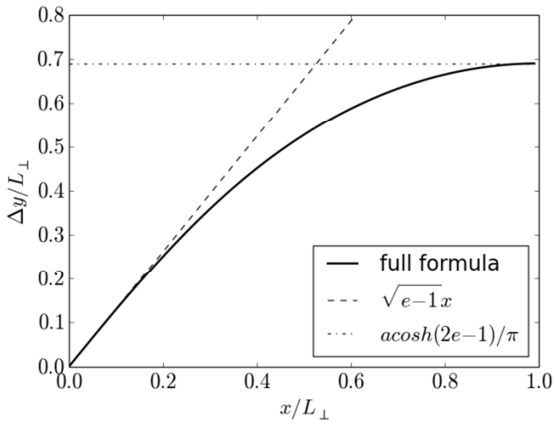

FIGURE 11. Half poloidal width at 1/e for G_{3D} at $\delta z_0=0$, from formula (37), versus $x/L_\perp$. Added are a linearized formula for $x/L_\perp<<1$ and the maximal value of the function

As the wave emission point moves away from the sheath wall, SW evanescence broadens G_{3D} in the poloidal direction. Formula (31) presents $G_{3D}(x,y,z_0)$ as the convolution of $\partial_z E_{3D}$ $(x',y,z=-L_{/\!/}/2,z_0)$ with $H(x,x',y)$. $\partial_z E_{3D}$ scales as $\sim R^{-5}$ for small R and as $\sim\exp(-R)$ for large R. An upper bound for its poloidal extent is therefore

$$L_{E\max}(x',\delta z_0)=\min\left[0.7L_x\sqrt{\left(\frac{\delta z_0}{L_z}\right)^2+\left(\frac{x'}{L_x}\right)^2},\,L_x\sqrt{1+2\sqrt{\left(\frac{\delta z_0}{L_z}\right)^2+\left(\frac{x'}{L_x}\right)^2}}\right] \qquad (38)$$

The poloidal half-width of H can be expressed explicitly as

$$L_H(x,x')=\operatorname{arccosh}\left[\frac{\sin(\pi x/L_\perp)\sin(\pi x'/L_\perp)}{\tanh[H(x,x',0)/e]}+\cos\left(\frac{\pi x}{L_\perp}\right)\cos\left(\frac{\pi x'}{L_\perp}\right)\right] \qquad (39)$$

L_H is an increasing function of $|x-x'|$. The source term for G_{3D} at point x is present from $x'=0$ to $x'=\min(x+L_x, L_\perp)$ (pessimistic estimate). One can then put an upper bound on the half-poloidal with for G_{3D}

$$\Delta y<\max[L_H(x,0),\,L_H(x,\min(x+L_x,L_\perp)),\,L_{Emax}(\min(x+L_x,L_\perp),\,\delta z_0)] \qquad (40)$$

The above estimates are assessed numerically on figure 12. In this exercise 2D (radial, poloidal) maps of G_{3D} at constant z_0 were simulated numerically over several scans of the main simulation parameters. From each map Δy was fitted at several radial positions. Over the

tested parametric domain inequality (40) is well verified, and the upper bound is sometimes pessimistic by a factor 2 or 3.

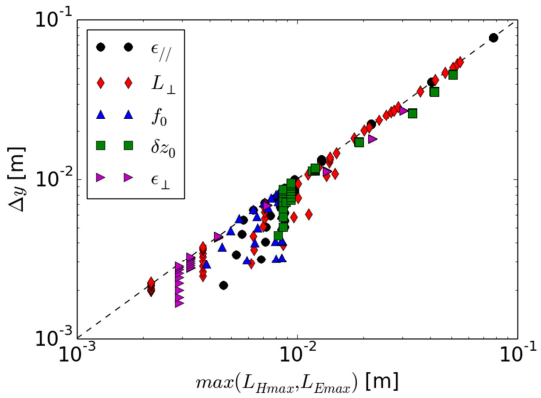

FIGURE 12. Half poloidal width Δy at 1/e, fitted numerically from simulated 2D (radial,poloidal) maps for G_{3D}. For each simulation Δy was fitted at 9 radial positions ranging from $x/L_\perp$=0.1 to 0.9 and plotted versus max(L_{Hmax}, L_{Emax}) from formula (40). Each series of points refers to a scan of one simulation parameter indicated in the legend.

For poloidal structures larger than max(L_{Hmax}, L_{Emax}) in the input field map, G_{3D} can be considerably simplified using (33).

$$G_{3D}(x,y,z_0) \approx G_{2D}(x,k_y=0,z_0)\delta(y) \qquad (41)$$

Surface integral (27) then reduces to a weighted integral along one single field line, located at the same altitude as the observation point. Consequently above a critical length, the poloidal structures of V_{RF} reflect those of $E_{//ap}$ near the parallel extremities of the input field map. Smaller scales below the critical length in the input RF field map are smoothed and contribute less to V_{RF}.

5. DISCUSSION AND CONCLUSION

5.1 Practical implications

Within the asymptotic SSWICH-SW model, RF oscillations V_{RF} of the sheath voltage at any open field line extremity can be expressed as a sum of individual contributions by each emitting point in the parallel RF electric field map $E_{//ap}(y_0, z_0)$ radiated by an IC antenna. This offers a simple alternative to the "double probe" criterion $\tilde{V}=|\int E_{//}.dl|$ for assessing sheath RF voltages closer to the first principles. For practical applications with realistic input field maps, the formalism developed here is generally less efficient numerically than the Fourier technique in [Colas2012] or the Finite Element Method in [Jacquot2014]. It allows however to reveal and quantify spatial proximity effects in the excitation of oscillating sheath voltages. Indeed, for the first time to our knowledge, proposed formula (3) consists of a *weighted* integral of $E_{//ap}$: Slow Wave (SW) evanescence causes point-source contributions (or Green's functions for V_{RF}) to decrease with increasing parallel and poloidal distances from wave

emission point to sheath walls. As a test case in a parallelepipedic box filled with homogeneous cold magnetized plasma, 2D and 3D Green's functions were determined explicitly in the limit of an emission point very close to the sheath walls, and their spatial variations were quantified numerically as a function of characteristic lengths in our model.

Poloidal decay lengths for V_{RF} involve the radial protrusion $L_\perp$ of antenna side limiters, as well as the transverse SW evanescence length L_x, with extra broadening due to the parallel evanescence. In realistic situations, these poloidal decay lengths are much lower than the typical vertical extent of ICRF antennas, e.g. less than 1.5cm for our ASDEX-Upgrade example. This is qualitatively consistent with experimental observations that RF-induced SOL modifications are mainly observed on magnetic field lines passing in front of the antenna box, while they are absent on field lines connecting above or below the box aperture [Jacquot2014], [Cziegler2012], [Kubič2013]. If poloidal structures in the input field map are larger than the decay length, independent 2D SSWICH-SW simulations at each altitude fairly approximate the full 3D models, while the 2D input RF field map retains 3D information about the global antenna geometry.

The parallel decay lengths for V_{RF} involve the minimum between the connection length $L_{//}$ and the parallel SW evanescence length L_z. The role of L_z was already pointed out in [Myra2010]. L_z is related to the transverse coupling of adjacent open magnetic field lines *via* $\varepsilon_\perp$ in equation 1. Such transverse coupling was absent in the "double probe" model. In SW propagation, decoupling is only obtained at the LH resonance ($\varepsilon_\perp$=0) and leads to infinite L_z. Typical parallel decay lengths are always smaller than typical antenna parallel extensions. Consequently, when the radiated $E_{//ap}$ map exhibits parallel anti-symmetry, an attenuation factor prevents the cancellation of the relevant integral for V_{RF} in equation (4). Sheath oscillations therefore persist with anti-symmetric strap toroidal phasing, while the previous formula predicts that $\int E_{//}.dl=0$. Besides, the sheaths at the two ends of the same open field line can oscillate differently, depending on the parallel symmetry of $E_{//ap}$ map. V_{RF} at an IC antenna side limiter appears mainly sensitive to $E_{//ap}$ emission by active or passive conducting elements near this limiter, as experimental observations suggest in [Colas2013] [Bobkov2015]. For the realistic simulations of ASDEX-Upgrade in [Křivská2015], a correlation was found between V_{RF} at antenna side limiters and RF field amplitudes at the same altitude, averaged over ~10cm from the side limiters along the parallel direction, whereas the antenna toroidal extension was 66cm. This correlation was independent of the altitude, of the antenna type and of the electrical settings, and mainly depended on the plasma

parameters. Toroidal proximity effects could therefore justify current attempts at reducing the local RF fields induced near antenna boxes to attenuate the sheath oscillations in their vicinity [Bobkov2015]. Although the proposed heuristic procedure does not fully coincide with our V_{RF}-cancellation rule, in both cases the optimal setting requires more power on the remote straps than on the close ones phased [0,π]. Since one cannot cancel V_{RF} everywhere on the antenna structure, one should carefully choose the spatial locations where to optimize RF-sheaths. Experiments in [Colas2013] and [Bobkov2015] showed that with two straps, improving the situation at one parallel side of the antenna box likely degrades the situation on the opposite side. Using a 3-strap antenna potentially removes this constraint [Bobkov2015].

In addition to the antenna geometry and its electrical settings, the V_{RF}-cancellation rule also involves the local plasma near the antennas, through the dielectric constants $\varepsilon_{//}$ and $\varepsilon_{\perp}$ governing the SW evanescence. Therefore replacing the plasma by a vacuum layer thicker than L_x in the radial direction could modify the optimal settings. This sensitivity, observed numerically in [Colas2005] [Milanesio2013] [Colas2014] [Lu2016a] [Jacquot2015], is a challenge for quantitative RF-sheath evaluations. Both L_x and L_z decrease with increasing local density near the antenna, which might help reducing the RF-sheath excitation. Although not modelled in this paper, a high local SOL density also eases Fast Wave coupling, resulting in lower RF field amplitudes at the aperture at given coupled power [Milanesio2013], [Lu2016a]. Experimentally, reduced Langmuir probe floating potentials were evidenced during ICRH at high SOL density on Tore Supra [Kubič2011]. High density operation was also used to reduce tungsten sputtering on ASDEX upgrade [Bobkov2010]. A major drawback at high SOL densities is however higher particle fluxes onto the antenna side limiters, with detrimental consequences on the heat loads [Colas2009], [Jacquet2011], [Jacquet2013], [Colas2014].

Although the above conclusions were reached in a parallelepipedic box filled with homogeneous plasma in the “wide sheath” limit, we believe that they persist qualitatively with more complex geometry, density gradients and finite sheath widths. Although Green’s functions are harder to determine in these more realistic situations, they still exist in any geometry and in presence of prescribed sheath widths, including the self-consitent sheath widths distribution, as long as the physics model remains linear. Within the asymptotic framework in [Colas2012], finite-sheath-width effects are small corrections to the “wide sheaths” solution. For Tore Supra, the fully-coupled simulation results with self-consistent sheath widths in [Jacquot2014] were found close in magnitude and spatial structure to the asymptotic first guess provided by the wide sheath approximation.

5.2 Physical limitations and prospects

The SSWICH-SW model predicts that the direct excitation of sheath oscillations by the evanescent SW is only intense in the IC antenna near RF field [Jacquot2014] [Colas2014] and loses efficiency beyond a parallel distance smaller than L_z from the radiating elements. The experiments in the introduction involved private limiters in this near field. However, RF-induced SOL modifications have often been observed experimentally at parallel distances far larger than L_z [Colas2013], [Bobkov2015], [Cziegler2012], [Klepper2013], [Kubič2013], [Lau2013], [Ochoukov2013]. To interpret these measurements, extra physical mechanisms not discussed in the present paper need to be considered.

In very tenuous SOLs below the lower hybrid resonance, the SW becomes propagative [Lu2016a] and can possibly excite RF sheaths at large parallel distances [Myra2008]. Propagative SW can be handled using the Green's function formalism introduced in this paper. However instead of decreasing monotonically with parallel and poloidal distances, the Green's functions may rather oscillate in a complex way.

At higher densities, the Fast Wave (FW) becomes propagative. It can excite so-called "far-field RF-sheaths" if $\mathbf{B_0}$ is not strictly normal to the walls [D'Ippolito2008] [Kohno2015]. The FW can also be incorporated into a generalized Green's function formalism in the "wide sheaths" asymptotic limit. For that purpose the asymptotic RF-sheath boundary conditions need to be extended to account for all RF field polarizations [D'Ippolito2006]. In addition to $E_{//ap,}$ the input RF field map should also include the radiated poloidal electric field. Each RF field component is expected to generate a specific Green's function. Evanescent FW likely exhibit proximity effects. But each polarization will feature specific characteristic decay lengths. Besides the wave equation for the FW cannot be recast into the generic form (6). Finally FW and SW will likely be coupled upon reflection onto tilted walls [D'Ippolito2008] [Kohno2015]. Extension of the SSWICH code to full-wave RF electric fields and shaped sheath walls in 2D is ongoing [Lu2016b].

While this paper discussed the sheath oscillating voltages V_{RF}, the deleterious effects in tokamaks ultimately arise from a local DC biasing of the SOL. The sheath rectification in step 3 of SSWICH is intrinsically non-linear and cannot be described with Green's functions. A transport of DC current likely couples one sheath with its neighbors and the one at the opposite extremity of the same open field line. In the absence of propagating RF waves, Jacquot's paper [Jacquot2014] showed that DC current transport can still spread a DC bias to remote areas from the near-field regions where SW direct sheath excitation is efficient. Along

this line of thought, in order to significantly reduce the rectified DC plasma potential on a given open field line, one should reduce $|V_{RF}|$ at its two extremities as well as on the neighboring field lines. Reducing $|V_{RF}|$ at only one extremity likely drives the circulation of DC current from the high-$|V_{RF}|$ sheath to the low-$|V_{RF}|$ sheath, with limited effects on the DC plasma potential [Jacquot2011].

A European project, outlined in [Colas2014], is ongoing to include all these extra physical mechanisms into more realistic models of coupled RF wave propagation and DC plasma biasing. Comparison with plasma measurements [Jacquot2014], [Křivská2015] proved essential for code assessment. The test of a new 3-strap antenna on ASDEX upgrade [Bobkov2015], the restart of the ITER-like antenna on JET [Durodié2012], the commissioning of new antennas on WEST [Hillairet2015], as well as dedicated test beds [Faudot2015] [Crombé2015] will provide new opportunities to assess the SSWICH model over a large diversity of antenna types and plasma regimes, before it can be used to predict the behavior of future antennas.

Acknowledgements. This work has been carried out within the framework of the EUROfusion Consortium and has received funding from the European research and training programme under grant agreement N° 633053. The views and opinions expressed herein do not necessarily reflect those of the European Commission.

REFERENCES

[Angot1972]: A. Angot, "Compléments de mathématiques", 6ème édition, Masson 1972 (in French)

[Bobkov2010] : V.V. Bobkov et al. *Nuclear Fusion* **50** (2010) 035004

[Bobkov2015] V. Bobkov et al., AIP Conf. Proc. **1689**, 030004-1 030004-8 (2015)

[Campergue2014]: A.-L. Campergue, P. Jacquet, V. Bobkov, D. Milanesio, I. Monakhov, L. Colas, G. Arnoux, M. Brix, A. Sirinelli and JET-EFDA Contributors, AIP Conf. Proc. **1580** p.263-266

[Chabert2011]: P. Chabert and N. Braithwaite. *Physics of Radio-Frequency plasmas*. Cambridge University Press, Cambridge, UK, 2011.

[Colas2005]: L. Colas, S. Heuraux, S. Brémond, G. Bosia, *Nucl. Fusion* **45** (2005) p.767–782

[Colas2009]: L. Colas, K. Vulliez, V. Basiuk and Tore Supra team, *Fusion Science and Technology* **56** 3 2009 pp 1173-1204

[Colas2012] L. Colas et al., *Phys. Plasmas* **19**, 092505 (2012)

[Colas2013] L. Colas et al., *Journal of Nuclear Materials* **438** (2013) S330–S333

[Colas2014] L. Colas et al., Proc. 21st IAEA FEC conference, St Petersburg (Russia) 2014, TH/P6-9

[Crombé2015]: Crombé, K. et al., *AIP Conference Proceedings*, **1689**, 030006 (2015)

[Cziegler2012] : Cziegler et al., *Plasma Physics and Controlled Fusion* **54** (2012) 105019

[D'Ippolito1998]: D.A. D'Ippolito, J.R. Myra et al. *Nuclear Fusion*, Vol. **38**, No. 10 (1998) p. 1543

[D'Ippolito2006]: D.A. D'Ippolito & J.R. Myra, *Phys. Plasmas* **13** 102508 (2006)

[Durand1966]: Durand E. 1966 « Electrostatique », tome 2 (Paris: Masson) p.265 (in French)

[Durodié2012]: F. Durodié et al., *Plasma Physics and Controlled Fusion* **54**, 074012 (2012)

[Faudot2013]: E. Faudot, et al. *Phys. Plasmas* **20** 043514 (2013)

[Faudot2015] E. Faudot, S. Devaux, J. Moritz, S. Heuraux, P. M. Cabrera, and F. Brochard, *Review of Scientific Instruments*, **86** 063502, 2015.

[Garrett2012]: M.L. Garrett, S.J. Wukitch, *Fusion Engineering and Design* **87** 2012 pp1570-1575

[Gradshteyn1980]: I.S. Gradshteyn & I.M. Ryzhik : "Table of Integrals, Series and Products", 4th edition, Academic Press (1980).

[Gunn2008]: J. P. Gunn et al., proc. 22nd Fusion Energy Conference, Geneva (2008) EX/P6-32

[Hillairet2015] : J. Hillairet et al., AIP Conf. Proc. **1689**, 070005-1 070005-8 (2015)

[Jacquet2011]: P. Jacquet et al., *Nuclear Fusion* **51** (2011) 103018

[Jacquet2013]: P. Jacquet et al., *Journal of Nuclear Materials* **438** (2013) S379–S383

[Jacquot2011]: J. Jacquot, L. Colas, S. Heuraux, M. Kubič, J.P. Gunn, E. Faudot, J. Hillairet, M. Goniche, "Self-consistent non-linear radio-frequency wave propagation and peripheral plasma biasing", proc. 19th topical conference on RF power in plasmas, Newport (RI) USA 2011, AIP conf. Proc. 1406, pp. 211-214

[Jacquot2014] J. Jacquot et al. *Phys. Plasmas* **21**, 061509 (2014)

[Jacquot2015] J. Jacquot et al., AIP Conf. Proc. **1689**, 050008-1 050008-4 (2015)

[Jenkins2015] T. G. Jenkins and D. N. Smithe, AIP Conf. Proc. **1689**, 030003-1 030003-8 (2016)

[Klepper2013] C. C. Klepper et al. *Journal of Nuclear Materials* **438** (2013) S594

[Kohno2012] H. Kohno et al. *Computer Physics Communications* **183** (2012) p. 2116

[Kohno2015]: H. Kohno et al., *Phys. Plasmas* **22**, 072504 (2015)

[Křivská2015] Křivská et al., AIP Conf. Proc. **1689**, 050002-1 050002-4 (2015)

[Kubič2011]: M. Kubič, J.P. Gunn, L. Colas, E. Faudot, S. Heuraux and A. Ngadjeu, proc. 38th EPS Conference on Plasma Physics Strasbourg ECA Vol. **35**G P2.074 (2011)

[Kubič2013]: M. Kubič, J.P. Gunn, S. Heuraux, L. Colas, E. Faudot, J. Jacquot, *Journal of Nuclear Materials* **438** (2013) S509–S512

[Lau2013] C. Lau et al. *Plasma Physics and Controlled Fusion* **55** 095003 2013

[Lerche2009] : E. A. Lerche et al., *AIP Conf. Proceedings* **1187** (2009) p.93

[Lu2016a] : L. Lu, K. Crombé, D. Van Eester, L. Colas, J. Jacquot and S. Heuraux, *Plasma Phys. Control. Fusion* **58** (2016) 055001

[Lu2016b]: L. Lu, L. Colas, J. Jacquot, B. Després, S. Heuraux, E. Faudot, D. Van Eester, K. Crombé, A. Křivská and J-M. Noterdaeme, "Non-linear radio frequency wave-sheath interaction in magnetized plasma edge: the role of the fast wave", proc. 43rd EPS conference on Plasma Physics, July 4th-8th 2016, Leuven, Belgium, poster P2.068

[Mendes2010]: A. Mendes et al., *Nuclear Fusion* **50** (2010) 025021

[MF1953]: Ph.M. Morse, H. Feshbach, "methods of theoretical physics", Mc. Graw Hill 1953

[Milanesio2009]: D. Milanesio , O. Meneghini, V. Lancellotti , R. Maggiora and G. Vecchi, *Nuclear Fusion* **49** (2009) 115019

[Milanesio2013]: D. Milanesio & R. Maggiora *Plasma Physics and Controlled Fusion* **55** (2013) 045010

[Myra2008]: Myra J.R. , D'Ippolito D.A. 2008 *Physical Review Letter* **101** 195004

[Myra2010]: J. R. Myra & D. A. D'Ippolito, *Plasma Physics and Controlled Fusion* **52** 015003 (2010)

[NGadjeu2011]: A. Ngadjeu et al. *JNM* **415** (2011) S1009

[Noterdaeme1993]: Noterdaeme J.-M. and Van Oost G. *Plasma Physics and Controlled Fusion* **35** (1993) p. 1481 and references therein.

[Ochoukov2013]: R. Ochoukov et al. *Journal of Nuclear Materials* **438** (2013) S875

[Perkins1989]: Perkins F.W., *Nuclear Fusion* **29** (4) 1989, p. 583

[Qin2013]: Q. M. Qin et al. *Plasma Physics and Controlled Fusion* **55** (2013) 015004

[Rozhansky1998]: V. A. Rozhansky, A. A. Ushakov, and S. P. Voskoboinikov, *Plasma Physics Reports* **24**, p.777 1998.

[Stix1992]: T.H. Stix, "Waves in Plasmas", AIP Press 1992

[VanNieuwenhove1992]: R. Van Nieuwenhove and G. Van Oost, *Plasma Physics and Controlled Fusion* **34** (4), 525–532 (1992)

[Wukitch2013]: S.J. Wukitch et al., *Physics of Plasmas* **20**, 056117 (2013)

Figures

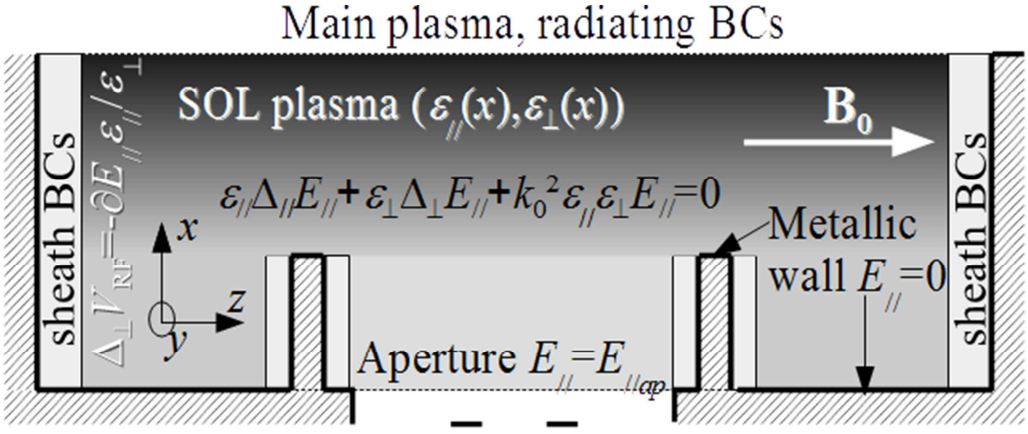

FIGURE 1: 2D (radial/parallel) cut into SSWICH general 3D simulation domain (not to scale). Main equations and notations used in the paper. The gray levels are indicative of the local plasma density. Light gray rectangles on boundaries normal to $\mathbf{B_0}$ feature the presence of sheaths, treated as boundary conditions in our formalism.

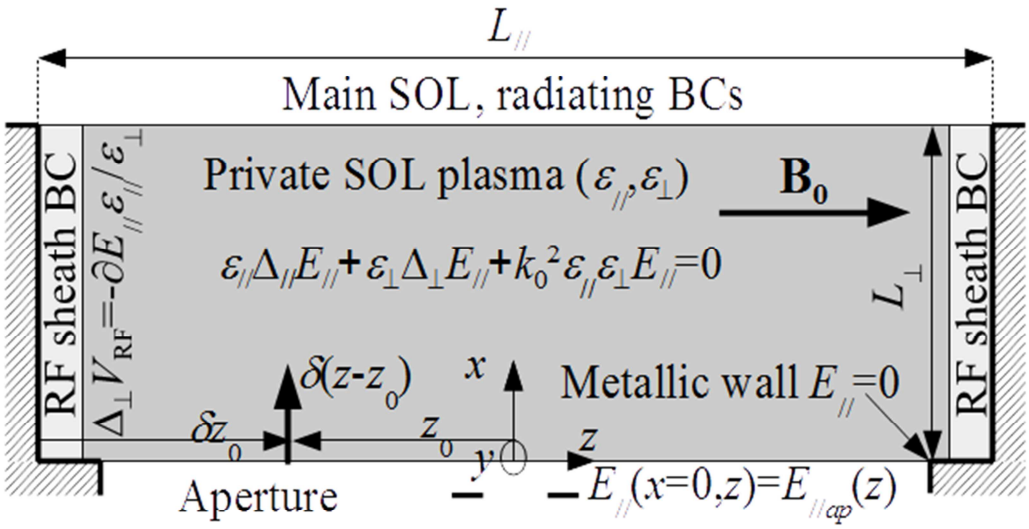

FIGURE 2: Generic 2D simulation domain (not to scale). Main equations and notations used in parts 3 and 4. x=0 at aperture. Light gray rectangles on boundaries normal to $\mathbf{B_0}$ feature the presence of sheath boundary conditions.

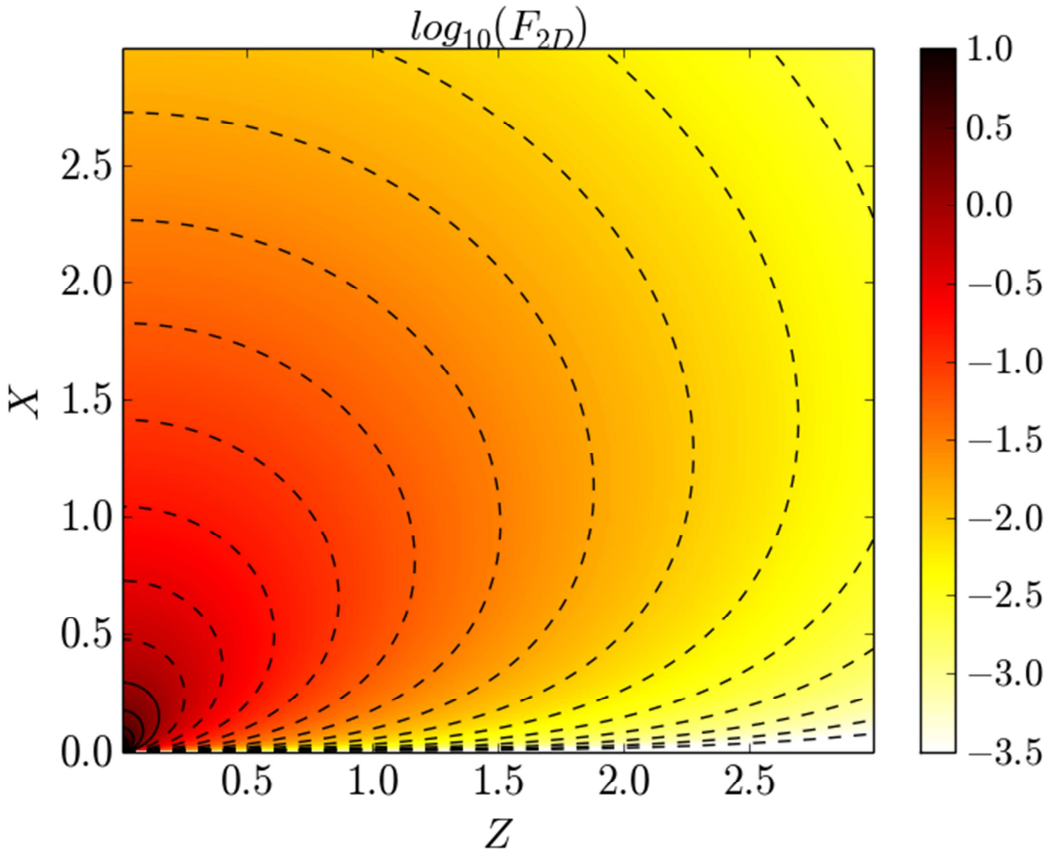

FIGURE 3. 2D plot of F_{2D}in logarithmic scale versus normalized coordinates (X,Z).

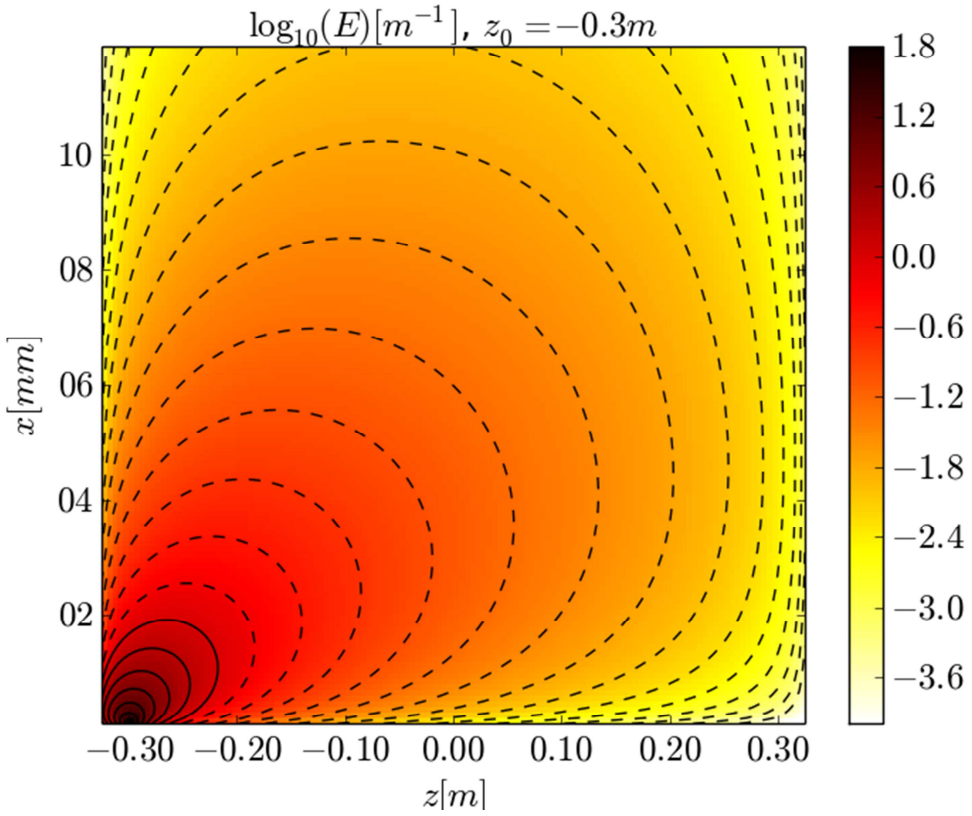
$\log_{10}(E)[m^{-1}]$, $z_0 = -0.3m$
10
08
06
04
02
$x[mm]$
−0.30 −0.20 −0.10 0.00 0.10 0.20 0.30
$z[m]$
1.8
1.2
0.6
0.0
−0.6
−1.2
−1.8
−2.4
−3.0
−3.6

a)

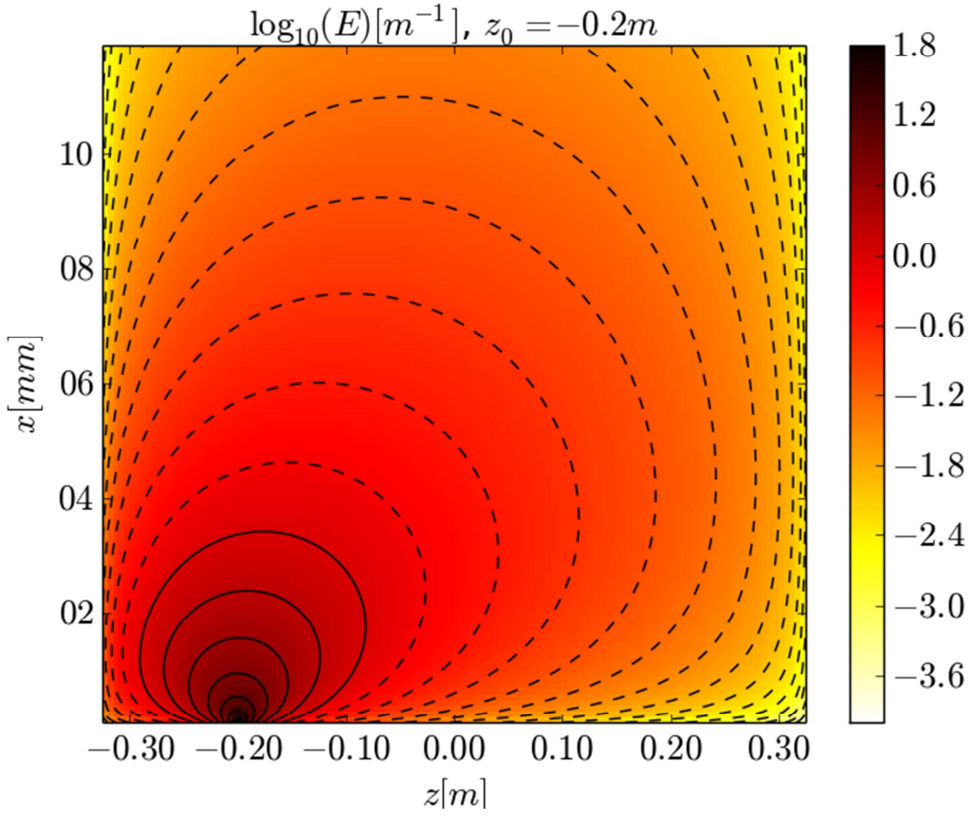
$\log_{10}(E)[m^{-1}]$, $z_0 = -0.2m$
10
08
06
04
02
$x[mm]$
−0.30 −0.20 −0.10 0.00 0.10 0.20 0.30
$z[m]$
1.8
1.2
0.6
0.0
−0.6
−1.2
−1.8
−2.4
−3.0
−3.6

b)

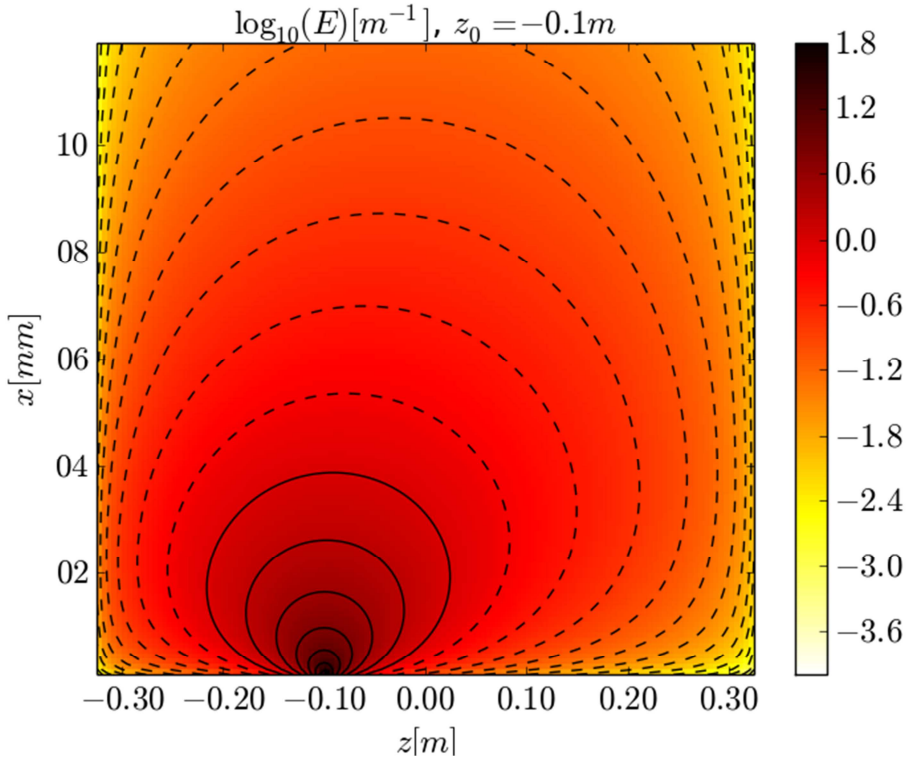

c)

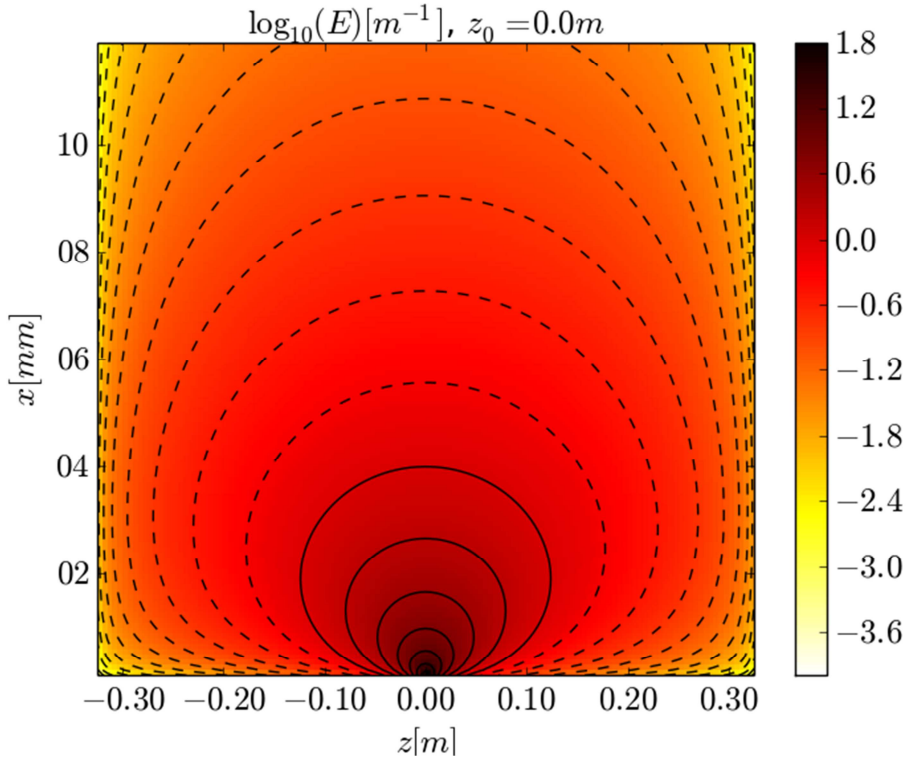

d)

FIGURE 4. 2D (parallel/radial) maps of $E_{2D}(x,z,z_0)$ in logarithmic scale, for ASDEX-Upgrade simulation parameters in [Křivská2015]and (a) z_0=-30cm; (b) z_0=-20cm; (c) z_0=-10cm; (d) z_0=0cm. x=0 corresponds to the antenna aperture, and x increases towards main plasma. z=0 is the mid-plane between antenna side limiters at z=±0.33m

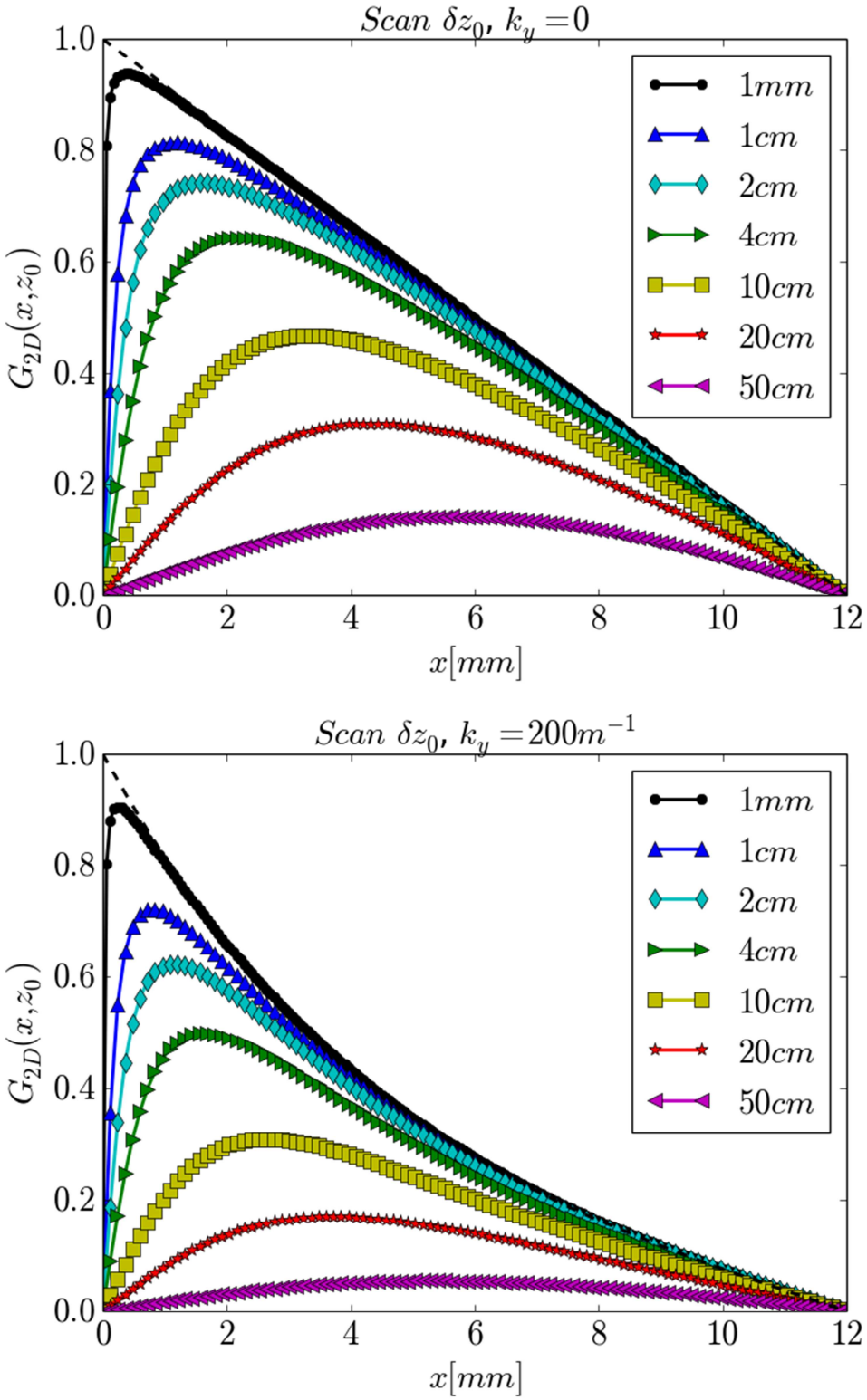

FIGURE 5. Green's function $G_{2D}(x,k_y,z_0)$ *versus* radial coordinate x for increasing parallel distance $\delta z_0=(L_{//}/2+z_0)$ from wave emission point $z=z_0$ to left parallel boundary $z=-L_{//}/2$. x is 0 at aperture and increases towards leading edge of antenna limiter at $x=L_{\perp}=12$mm. Simulation with ASDEX-Upgrade parameters used in [Křivská2015] and (a) $k_y=0$, (b) $k_y=200\text{m}^{-1}$. Dashed lines: asymptotic expression (21).

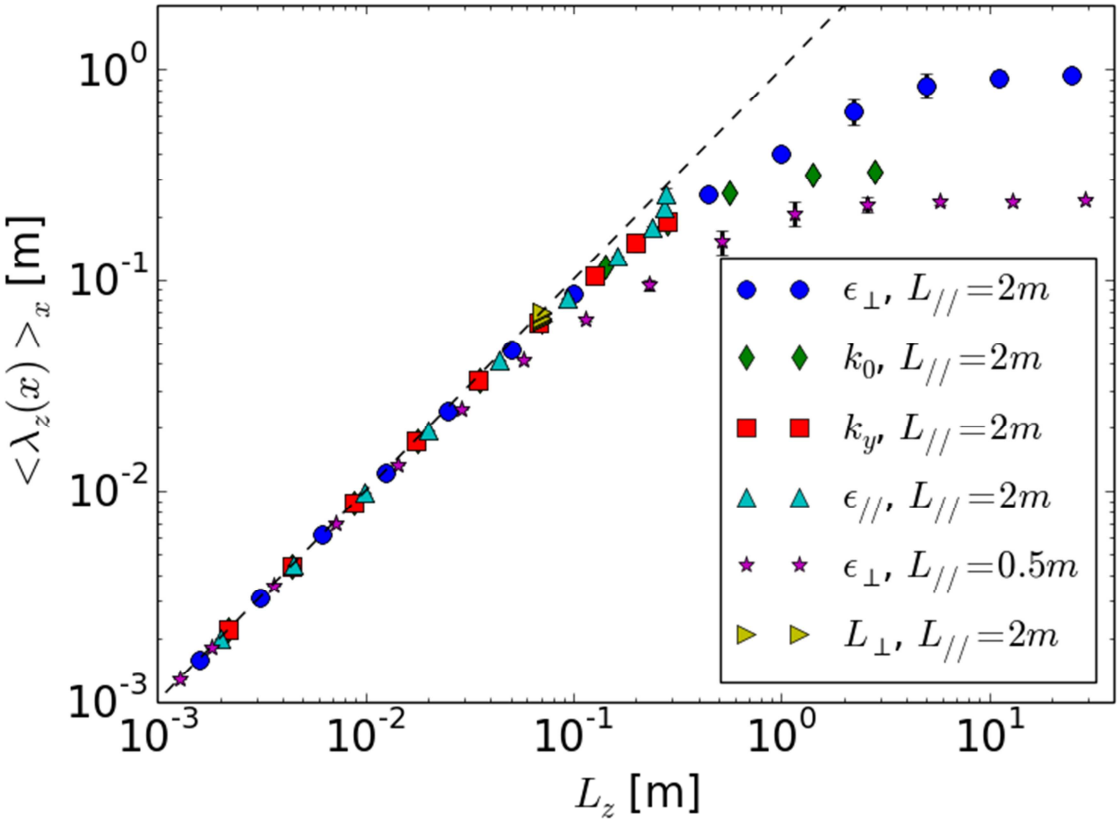

FIGURE 6. Parallel e-fold decay length $\lambda_z(x)$ of $G_{2D}(x,k_y,z_0)$ at $z_0=0$ fitted numerically and averaged over 20 values of x, versus L_z from eq. (5), for 6 scans of the main parameters in the asymptotic model, each identified by a marker type. Error bars: dispersion of $\lambda_z(x)$ over x.

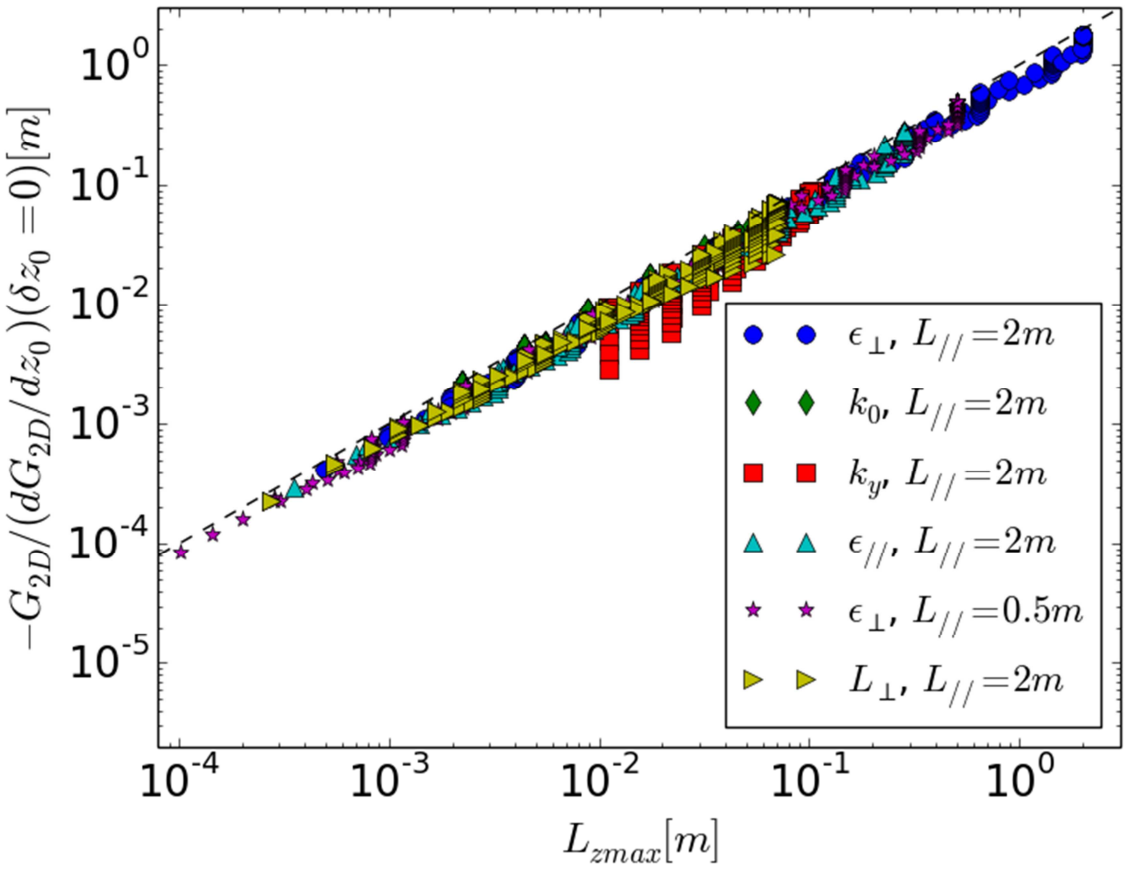

FIGURE 7. Parallel gradient length of $G_{2D}(x,k_y,z_0)$ fitted numerically at $\delta z_0=0$, *versus* upper bound L_{zmax} from eq. (26). For each simulation, 19 points are plotted, for x values located every 5% of $L_\perp$. Marker types indicate simulation series with one parameter scanned.

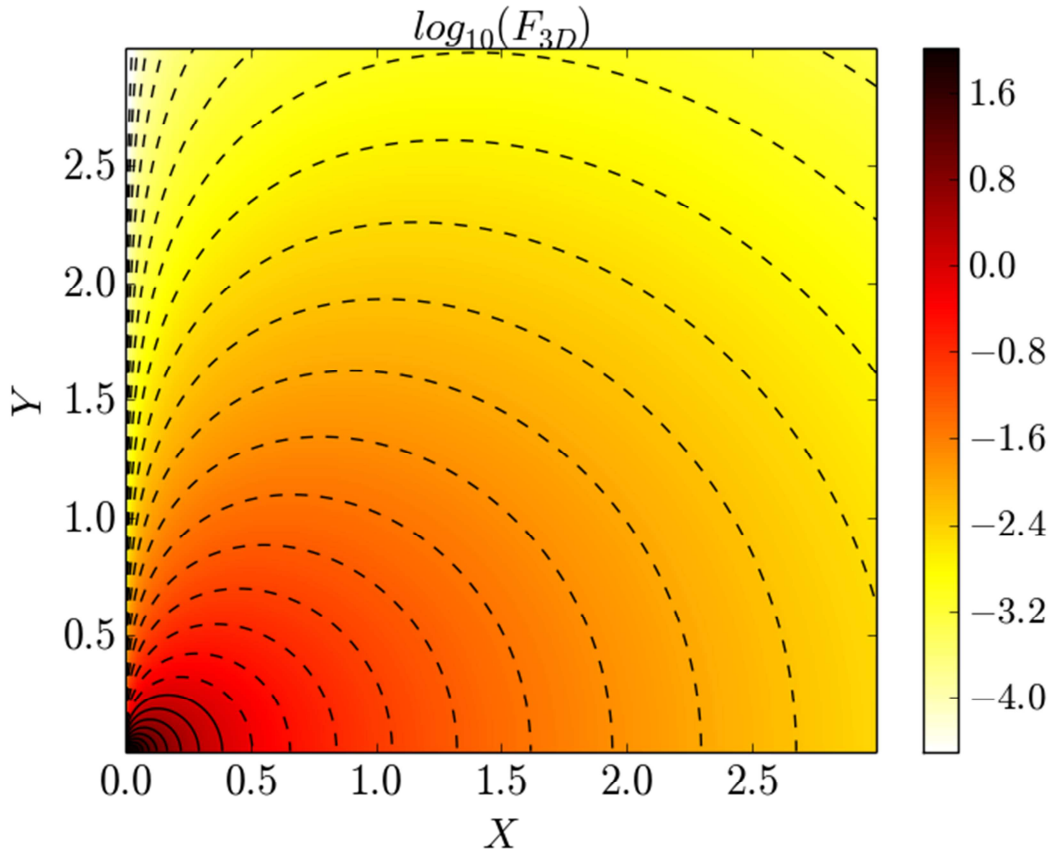

FIGURE 8. 2D (radial, poloidal) map of $F_{3D}(X,Y,Z=0)$ from formula (29) in logarithmic scale, versus normalized transverse coordinates (X, Y).

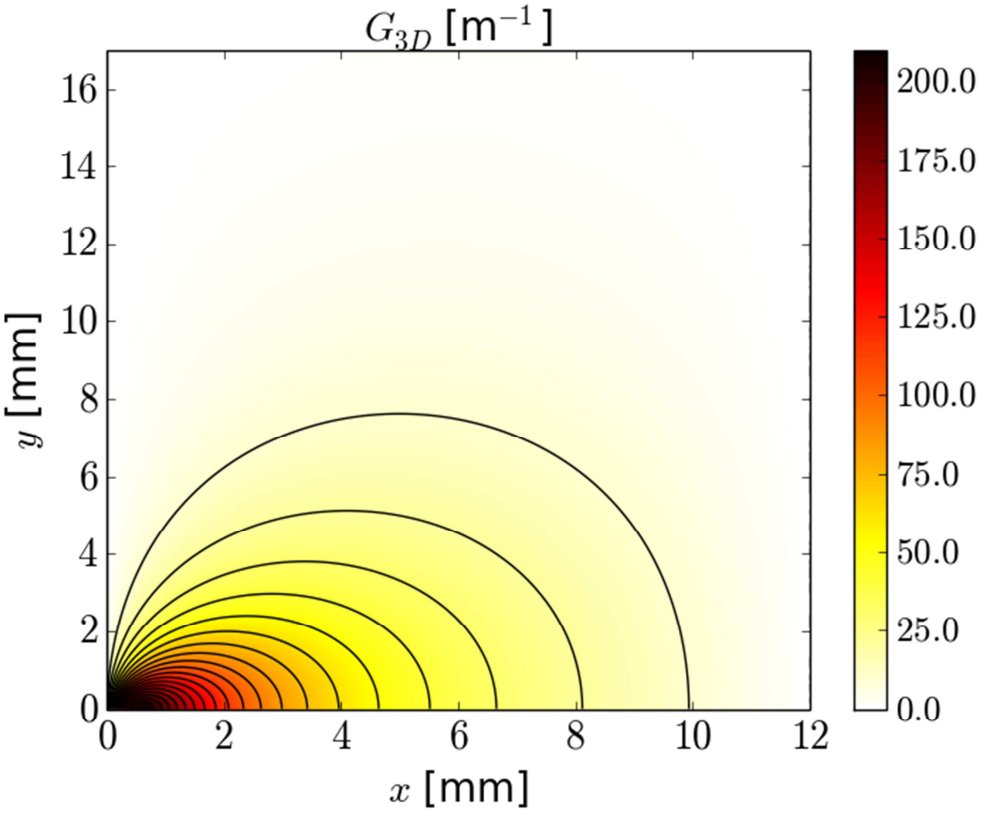
G_{3D} [m^{-1}]
y [mm]
x [mm]
0
2
4
6
8
10
12
14
16
200.0
175.0
150.0
125.0
100.0
75.0
50.0
25.0
0.0

a)

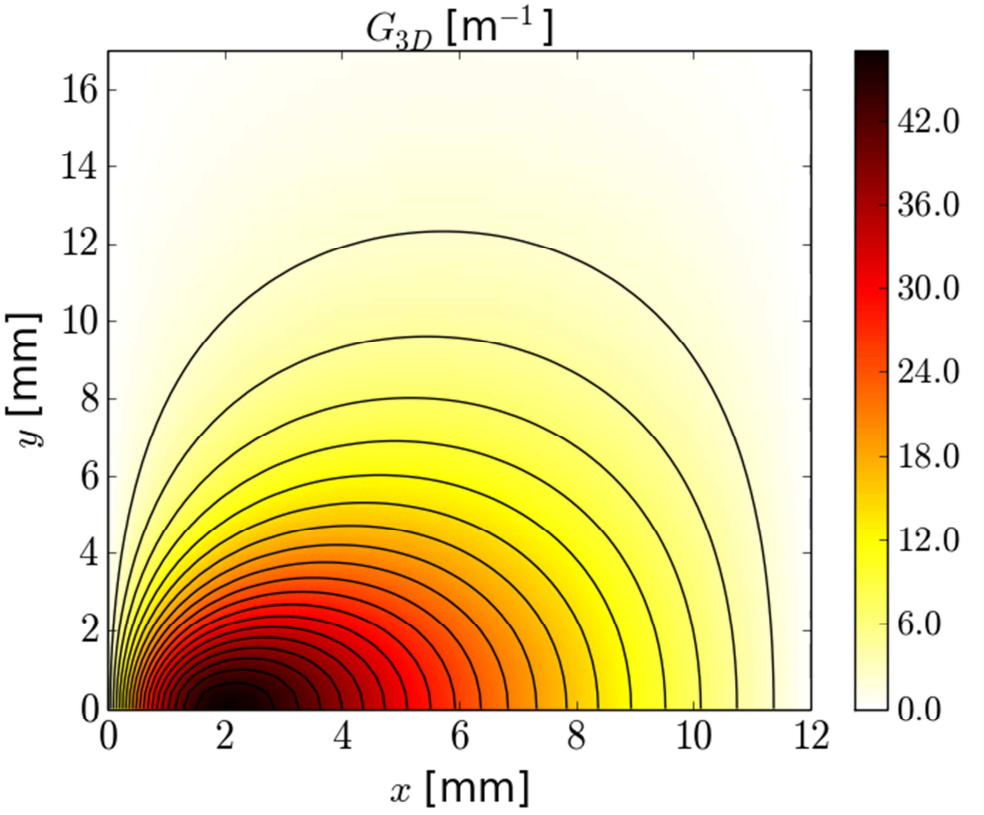
G_{3D} [m^{-1}]
y [mm]
x [mm]
0
2
4
6
8
10
12
14
16
42.0
36.0
30.0
24.0
18.0
12.0
6.0
0.0

b)

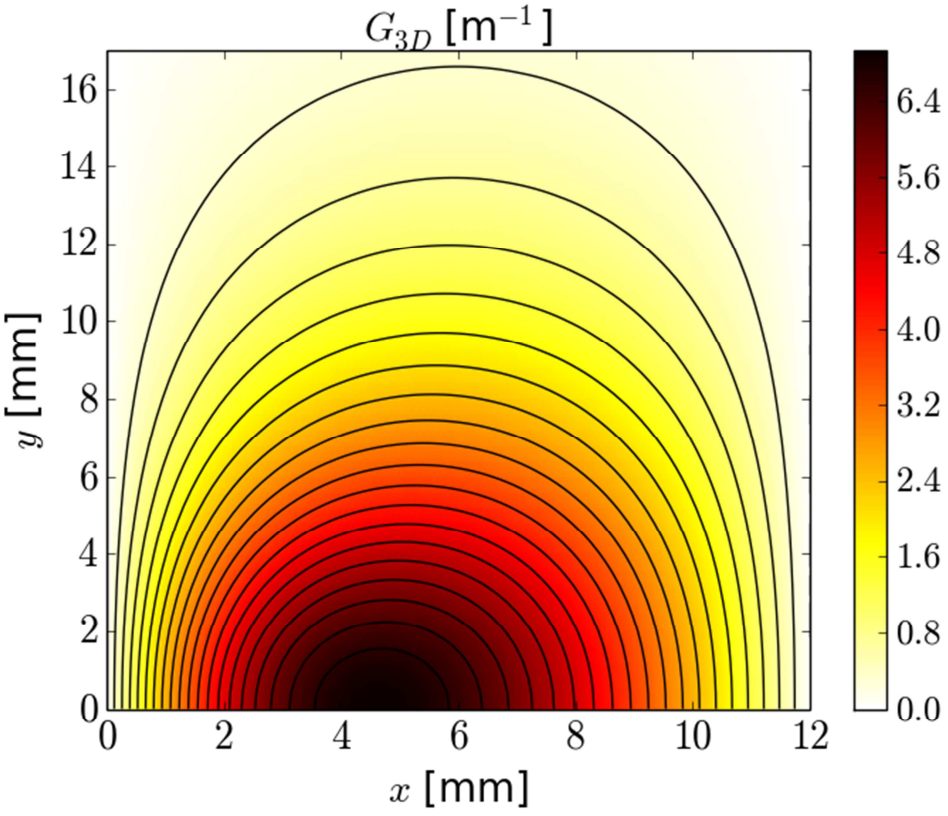

c)

FIGURE 9. 3D Green's function $G_{3D}(x,y,z_0)$ *versus* transverse coordinates (x,y), as evaluated numerically using ASDEX-Upgrade simulation parameters in [Křivská2015] and parallel distances (a) $\delta z_0=(L_{//}/2+z_0)=2.5$cm; (b) $\delta z_0=10$cm and (c) $\delta z_0=33$cm. Contour lines are located every 5% of the maximum value over the map.

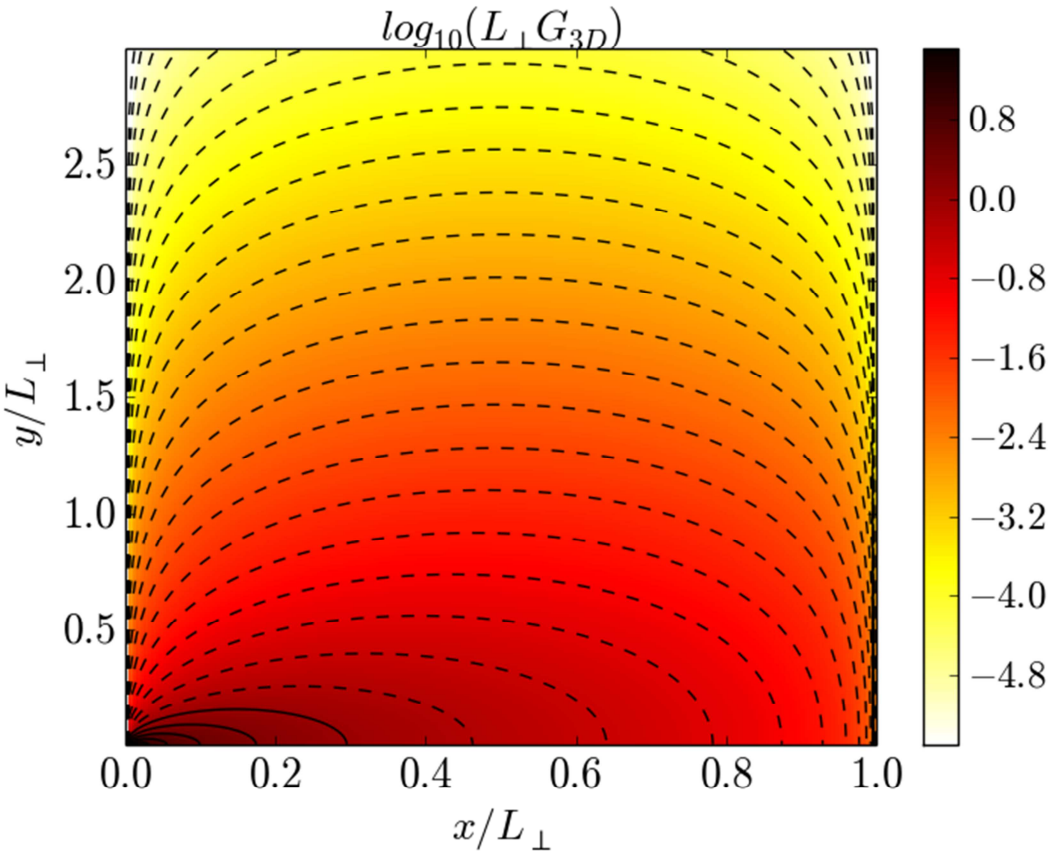

FIGURE 10. 2D (radial, poloidal) map of $L_\perp G_{3D}(x,y,-L_{//}/2)$ from formula (34) in logarithmic scale, versus normalized coordinates ($x/L_\perp$, $y/L_\perp$).

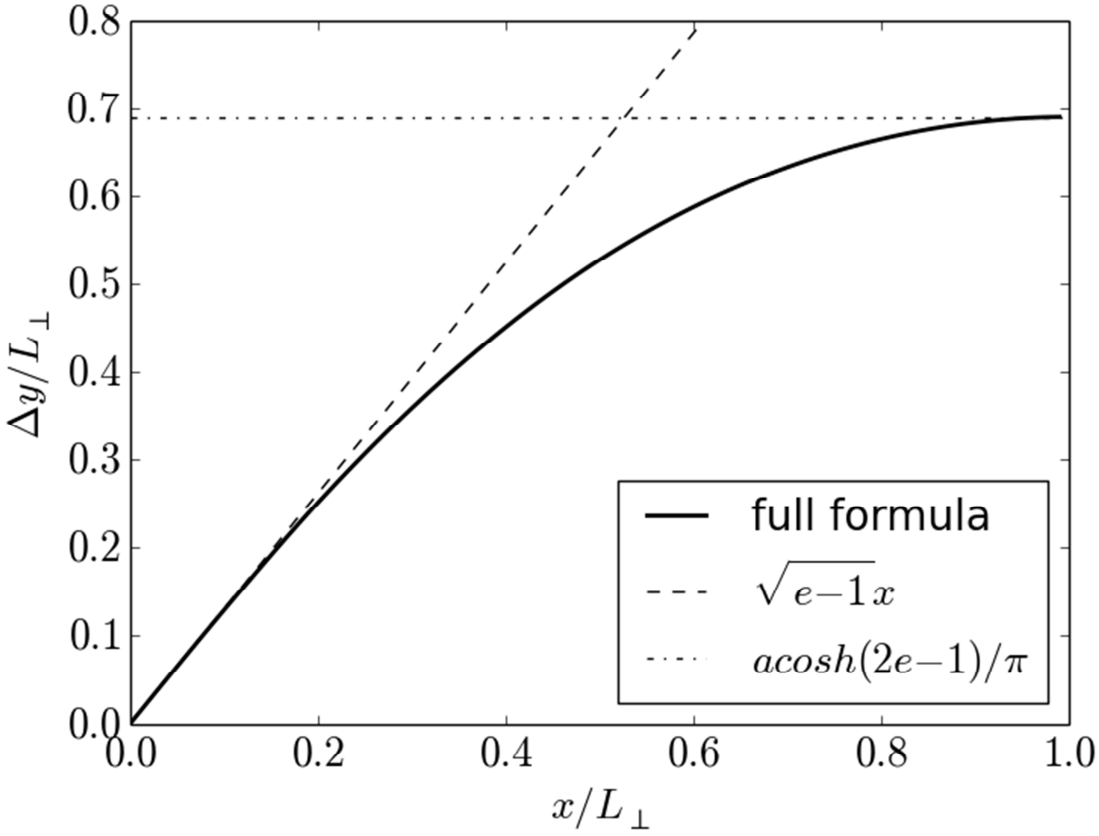

FIGURE 11. Half poloidal width at 1/e for G_{3D} at δz_0=0, from formula (37), versus $x/L_\perp$. Added are a linearized formula for $x/L_\perp$<<1 and the maximal value of the function

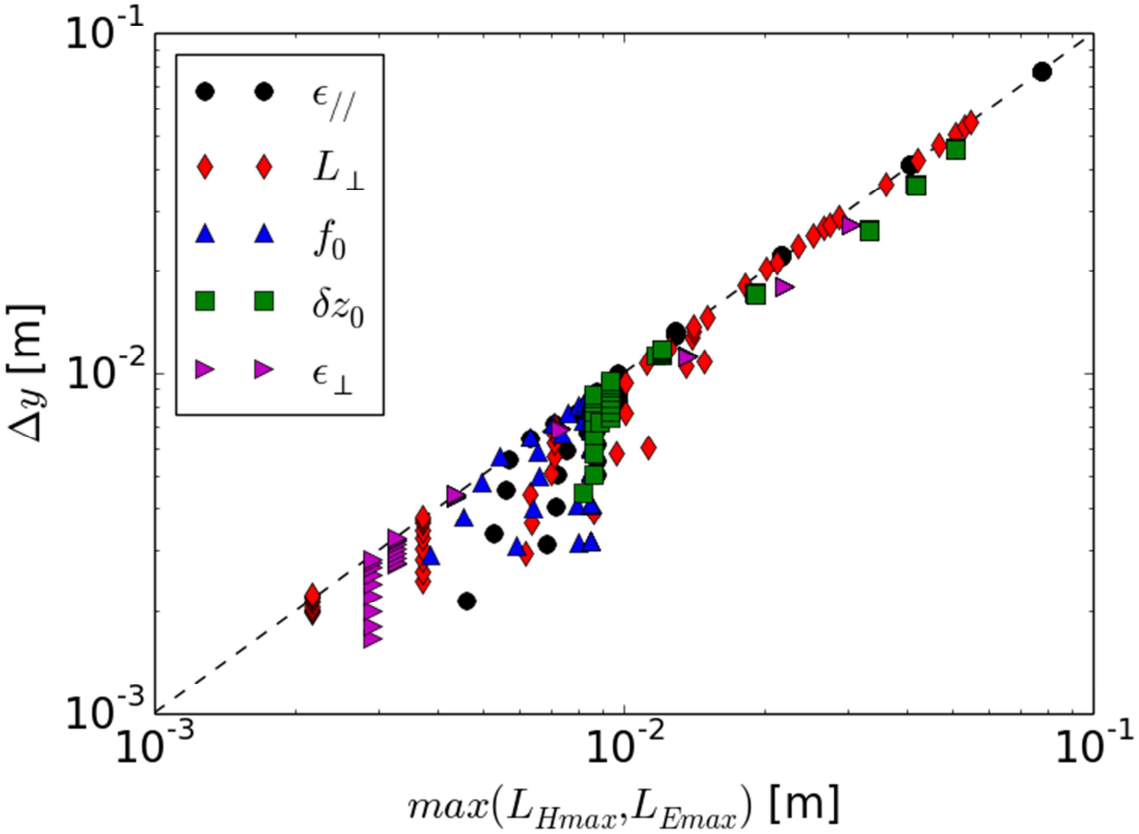

FIGURE 12. Half poloidal width Δy at 1/e, fitted numerically from simulated 2D (radial,poloidal) maps for G_{3D}. For each simulation Δy was fitted at 9 radial positions ranging from $x/L_\perp$=0.1 to 0.9 and plotted versus max(L_{Hmax}, L_{Emax}) from formula (40). Each series of points refers to a scan of one simulation parameter indicated in the legend.